Dalton Transactions

ROYAL SOCIETY OF CHEMISTRY

PAPER

View Article Online
View Journal | View Issue

Cite this: *Dalton Trans.*, 2024, **53**, 8662

DLPNO-CCSD(T) and DFT study of the acetate-assisted C–H activation of benzaldimine at $[RuCl_2(p\text{-cymene})]_2$: the relevance of ligand exchange processes at ruthenium(II) complexes in polar protic media†

Vicente Ojea * and María Ruiz

To gain mechanistic insights into the acetate-assisted cyclometallations of arylimines promoted by $[RuCl_2(p\text{-cymene})]_2$ in polar protic media, DFT geometry optimizations (with M06 and ωB97X-D3 functionals and the cc-pVDZ-PP[Ru] basis set) followed by DLPNO-CCSD(T)/CBS energy evaluations were performed using benzaldimine as a model substrate and methanol as the solvent (with CPCM or SMD models). The calculation results show that coordination of the imine to an acetate ruthenium precursor is followed by anion (chloride or acetate) dissociation as the rate-determining step of the process. H-Bonding of two explicit MeOH to the anion reduces the calculated activation energy to *ca.* 23 kcal mol^{-1}, in good agreement with the experimental half-life at room temperature. Subsequent AMLA/CMD C–H activation of the intermediate cationic complexes is a faster, reversible process. Alternative reaction pathways involving neutral diacetate ruthenium complexes offer AMLA/CMD transition state structures of lower energy but are precluded due to higher energy barriers for the initial ligand exchange processes at ruthenium. Solvent assistance accelerates the final chloride/acetate exchange processes on the cycloruthenate intermediates, particularly when compression in the condensed phase is taken into consideration. The performance of six DFT functionals (with the aug-pVTZ-PP[Ru] basis set) was assessed using the DLPNO-CCSD(T)/CBS reference energies. Neutral diacetate ruthenium complexes were incorrectly predicted as being kinetically relevant when using hybrid DFT methods (PBE0-D3(BJ), M06-2X or ωB97M-V). Good agreement between the calculated barrier heights and our benchmark energy results was obtained by using double-hybrid DFT methods. PWPB95 with D3(BJ) or D4 dispersion energy corrections was found to be the most accurate ($\Delta G^{\neq}$ MUE of *ca.* 1 kcal mol^{-1}). This study may aid our understanding of and help with further experimental investigations of synthetically useful carboxylate-assisted C–H bond functionalizations involving (*N*,*C*)-cyclometallated (*p*-cymene)Ru(II) intermediate complexes in sustainable polar protic solvents.

Received 7th February 2024,
Accepted 19th April 2024

DOI: 10.1039/d4dt00380b

rsc.li/dalton

1. Introduction

Transition-metal-catalyzed C–H bond functionalizations have emerged as essential tools in organic synthesis. Among widely used transition metals, ruthenium has powerful advantages for C–H activations, including high versatility, broad functional group tolerance, and relatively low cost.[1] In particular, carboxylate-assisted ruthenium(II) catalysis constitutes a reliable tool for either directed or nondirected C–H activations.[2] These features have enabled the employment of non-hazardous, renewable, and environmentally benign solvents for the development of sustainable ruthenium(II)-catalyzed C–H functionalizations.[3]

Chelation assistance has proved instrumental for enhancing the site-selectivity of ruthenium catalyzed C–H activation and functionalization. The transformation requires binding of a directing group (DG) to the metal center, formation of a key ruthenacyclic intermediate and subsequent functionalization or annulation. Heterocycles with a strongly coordinating nitrogen atom (pyridine, oxazoline, pyrazole...) have been successfully utilized as DGs in these aromatic C–H bond transformations (see Scheme 1). In many of these processes $[RuCl_2(p\text{-cymene})]_2$ was revealed as an optimal, bench-stable, commer-

Departamento de Química, Facultade de Ciencias, Universidade da Coruña, E-15078 A Coruña, Spain. E-mail: vicente.ojea@udc.es

†Electronic supplementary information (ESI) available: Additional Chart, Figures, and Tables; Rationale for the selection of methods; Computational methods; Computed cartesian coordinates, lowest frequencies, and energies. See DOI: https://doi.org/10.1039/d4dt00380b

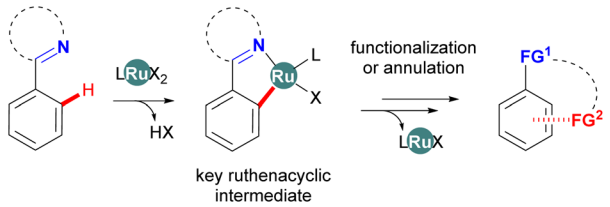

Scheme 1 Ruthenium(II) catalyzed C–H functionalization or annulation of arenes equipped with N-containing DGs. L stands for η^6-arene co-ligand and X for carboxylate or chloride.

cial catalyst precursor.[4] Moreover, many cyclometallated (*p*-cymene)Ru(II)-complexes formed in this way could be isolated[5] and were shown to be key intermediates and catalytic species[6] for the functionalization of arenes. Since many of the *N*-containing heterocycles, such as aryl substituted pyridines, may be difficult to modify or remove, the use of imines constitutes a more efficient synthetic alternative. Imines are readily accessible, inexpensive, can undergo a variety of chemical transformations and prove to be one of the most efficient transient DGs reported to date in transition-metal-catalyzed functionalizations.[7] Thus, following on from an early report by Oi and Inoue,[8a] efficient arylations,[5c,8b,c] alkylations,[7d,9] annulations[10] and amidations[11] of arylimines by carboxylate-assisted (arene)ruthenium(II) catalysis have been developed. Moreover, recent examples reveal the convenience of employing polar protic solvents, such as alcohols[7e,10b,c] or water[8c] in such functionalizations to achieve efficiency and sustainability improvements.

Different mechanistic possibilities have been considered for the activation of C–H bonds by transition metal complexes.[12] The generally accepted proposal for carboxylate-assisted C–H activations involves coordination of the substrate to the electrophilic metal to form a complex with increased acidity that facilitates subsequent deprotonation by a carboxylate group in either an intra- or intermolecular[13] fashion (see Chart 1). When cleavage of the C–H bond and formation of the carbon–metal bond take place in a concerted fashion, frequently involving a 6-membered transition state (TS), the process is known as "concerted metalation–deprotonation"[14] (CMD) or "ambiphilic metal-ligand assistance"[12a,15] (AMLA).[16]

Most of the current knowledge of the mechanism of carboxylate-assisted C–H activations by ruthenium(II) complexes is based on computational evidence.[17] DFT studies covering the reactions of phenylpyrazoles,[18] benzylamines,[19] phenylpyridines,[20] *N*-aryl-oxazolidinones,[21] naphthols,[22] aryl carboxylic acids,[23] arylphosphonates,[24] arylacetamides,[16d,25] benzamides,[26] pyridylindoles,[27] phenylketones,[28] hydroxy-chromones[29] or phenylimidazoles[30] promoted by $[RuCl_2(p\text{-cymene})]_2$ and acetate anions (or preformed $Ru(OAc)_2(p\text{-cymene})$) support initial substrate (**A**) binding to the ruthenium precursor (**B**) followed by dissociation of a ligand (from **C**) and creation of a key intermediate with a vacant site at which the M–C bond can form (see Scheme 2). Most of these electrophilic intermediates are cationic in nature ($\mathbf{D}^+$)[31] but alternative routes involving neutral intermediates equipped with two acetate ligands bound to the ruthenium ($\mathbf{F}^L$) and showing η^6–η^2 slippage[32] or substitution of the arene co-ligand

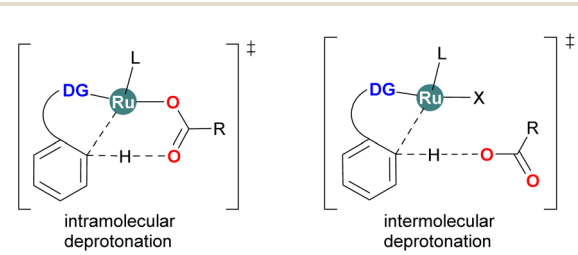

Chart 1 AMLA/CMD TS structures for carboxylate-assisted ruthenation of C–H bonds. DG stands for directing group, L stands for η^6-arene co-ligand and X for carboxylate or chloride.

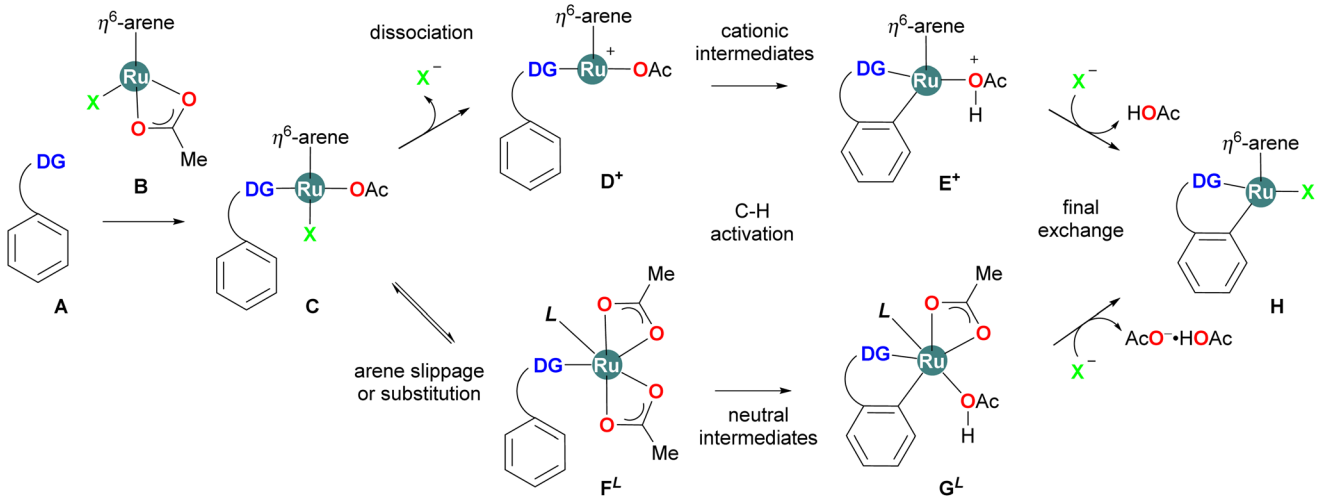

Scheme 2 Routes involving cationic and neutral intermediates for C–H activation at Ru(II)(arene) complexes. DG stands for directing group, X stands for chloro or acetate, L stands for arene, solvent or substrate as η^2-ligands.

by solvent or a second substrate molecule[33] have been also reported. From either cationic or neutral intermediates the C–H activation event (to $\mathbf{E}^{+}$ or $\mathbf{G}^{\mathbf{L}}$, respectively) is followed by final HOAc exchange to form a stable cycloruthenate complex (**H**) or enable a subsequent functionalization process. In some of these DFT studies the C–H activation events were claimed to be rate determining[5g,18,20b,21,23e,24,26d] although transition states for initial anion dissociation, ligand substitution or final HOAc exchange at ruthenium were not located and the corresponding energy barriers were assumed to be diffusion-controlled.[34] Thus, the potential kinetic relevance of ligand exchange processes at ruthenium has been overlooked and further quantum mechanical calculations on carboxylate-assisted C–H activations by ruthenium(II) complexes are required.

Although a number of examples of stoichiometric or catalytic C–H bond activations and functionalizations of arenes equipped with *N*-containing DGs by ruthenium(II) are present in the literature,[4–9] to the best of our knowledge, no computational studies have been disclosed for the cyclometallation of arylimines or for the involvement of discrete molecules of polar protic solvents in directed C–H bond activation events promoted by Ru(II)(*p*-cymene) complexes.[35,36] Thus, herein we introduce a detailed computational study of the cyclometallation of *N*-phenyl benzaldimine (**A**) promoted by $[RuCl_2(p\text{-cymene})]_2$ ($\mathbf{B}^{\mathbf{0}}$) and acetate anions in methanol. The main aims of the study are directed to the evaluation of reaction pathways involving cationic or neutral electrophilic ruthenium species in the C–H activation process, the identification of the rate-determining step (RDS) and the establishment of the prevalence of kinetic or thermodynamic control for the global process. For these purposes the effect of the polar protic solvent on geometry optimizations and energy evaluations has also been considered. In addition, selected hybrid and double-hybrid DFT methods among the top performers in the MOR41 and MOBH35 databases[37] were evaluated against our benchmark results to localize an accurate scheme of reduced computational cost for the study of the thermodynamics and kinetics of these cyclometallation processes. Our calculations in methanol as a solvent show that the C–H activation event is reversible and kinetically irrelevant and that the rate of cyclometallation should be determined by ligand exchange processes at the ruthenium intermediate complexes.

2. Results and discussion

Calculations reported in this paper were performed for the model system shown in Scheme 3, that is, the reaction of **A** with stoichiometric $\mathbf{B}^{\mathbf{0}}$ in the presence of 2 equivalents of acetate anions (sodium cations were excluded) leading to chloro ruthenacycle **H**. The computational protocol involved geometry optimizations using M06[38] and ωB97X-D3[39] functionals in combination with a polarized double-ζ basis set and an effective core potential for ruthenium (cc-pVDZ-PP[Ru]) followed by highly accurate yet computationally efficient energy evaluations with an approximate local coupled-cluster

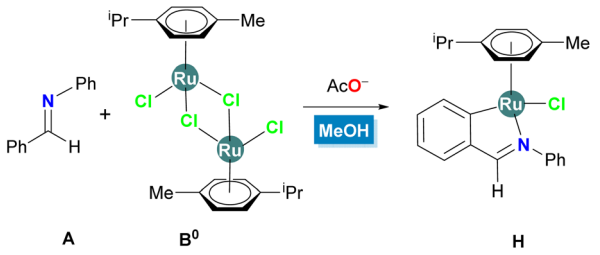

Scheme 3 Model reaction system under study.

method[40] and extrapolation to the complete basis set limit (DLPNO-CCSD(T)/CBS level).[41] The influence of the polar protic solvent on the geometry optimization process and final energy evaluations have been considered with a hybrid explicit–implicit solvent model,[42] by using polarizable continuum solvation models (CPCM and SMD)[43] but also including explicit molecules of MeOH. The discussion of the theoretical calculations is presented in terms of the quasi-harmonic[44] Gibbs energies in methanol at 298 K corrected for the change from the gas phase (1 atm) to two different standard states in solution (with either a solute concentration of 1.0 M or a liquid methanol concentration of 24.6 M) to better reflect the experimental conditions (see Rationale for the selection of methods and Computational methods in the ESI† for further details). To enable a comparison of the competitive reaction channels the ruthenium dimeric precursor $\mathbf{B}^{\mathbf{0}}$, imine **A**, acetate and an adequate number of methanol molecules were taken separately as zero for the quasi-harmonic Gibbs energies. Throughout the whole article, the difference in Gibbs energy between an intermediate or TS structure and the global reference is abbreviated to ΔG_r.

This work is divided into four sections. The first one is related to the pre-activation of ruthenium precursors and the formation of key electrophilic intermediates. The second section describes the C–H activation event and the third one the final ligand exchange processes at the most significant ruthenacyclic intermediate. In the fourth section the competence between reaction pathways is discussed and the lowest energy profile and the RDS are uncovered. The fourth section is divided into three subsections that include separate analyses of the results obtained using the CPCM or SMD solvation models and a final comparison with the experimental results that supports the computational results. In the first, second and third sections, energy barriers and relative Gibbs energies calculated at the DLPNO-CCSD(T)/CBS(CPCM) level after geometry optimizations with the M06 functional are reported first, followed by the corresponding values, between brackets, calculated at the same level on the ωB97X-D3 geometries. For comparison purposes, a third set of energy values calculated at the DLPNO-CCSD(T)/CBS(SMD) level on the ωB97X-D3 geometries are reported last, in brackets and italics.

2.1. Pre-activation by anion dissociation and ligand exchange processes at ruthenium

The reaction of the dimeric dichloro(*p*-cymene)ruthenium precursor ($\mathbf{B}^{\mathbf{0}}$) with acetate in methanol was studied first. Kinetic

evidence reported by Bassetti *et al.*[45] indicates that this process should be initiated by ruthenium–chloro bond breaking, release of chloride and the formation of a cationic intermediate (see $\mathbf{B^{0+}}$ in Scheme S2 of the ESI†). Such a dissociation process was calculated to be endergonic by 2.7 [0.9] kcal mol^{-1} and showed an activation energy of 20.2 [18.9] kcal mol^{-1}. Next, acetate/chloride exchange processes also take place easily on ruthenium at room temperature, to give chloro–acetate derivative $\mathbf{B^1}$ and diacetate derivative $\mathbf{B^2}$ as key cyclometallation promoters (see Chart 2).

Formation of chloro–acetate derivative $\mathbf{B^1}$ from ruthenium dimeric precursor $\mathbf{B^0}$ was calculated to be exergonic by 8.3 [9.0] [*2.8*] kcal mol^{-1} while diacetate derivative $\mathbf{B^2}$ lies at −11.9 [−12.0] [*2.1*] kcal mol^{-1}. Solvent-assisted dissociation of $\mathbf{B^1}$ or $\mathbf{B^2}$ led to the solvated ($\mathbf{B^{+S}}$) and the unsolvated ($\mathbf{B^+}$) cationic precursors, which were characterized to be higher in energy than the starting compounds, at 5.6 [5.8] and 21.7 [19.1] kcal mol^{-1}, respectively. Solvent-assisted dissociation of $\mathbf{B^2}$ to form free *p*-cymene and mono-, di- or tri-solvated Ru(OAc)$_2$ complexes was calculated to be endergonic by more than 25 kcal mol^{-1} (see ESI, Scheme S3†). These results are consistent with the intermediate species identified by ^{1}H NMR in the cyclometallations of 2-arylquinazolines with [RuCl$_2$(*p*-cymene)]$_2$ and KOAc in MeOH as the solvent.[5e]

Binding of ligand **A** to monomeric precursors $\mathbf{B^1}$ or $\mathbf{B^2}$ takes place by coordination of the nitrogen atom to ruthenium (see Scheme 4, entry a). Such coordination processes involve TS structures $\mathbf{TS(B^1\text{-}C^1)}$ or $\mathbf{TS(B^2\text{-}C^2)}$ located at 8.5 and 6.4 [9.7 and 6.6] [*19.3* and *16.9*] kcal mol^{-1} and give rise to the chloro–acetate complex $\mathbf{C^1}$ or diacetate complex $\mathbf{C^2}$ which were found at 0.2 and −5.8 [−4.1 and −4.8] [*2.4* and *4.7*] kcal mol^{-1}, respectively. The loss of an anion from the tetracoordinate ruthenium intermediates gives rise to the key cationic intermediate, with a vacant coordination site available at the metal. Dissociation of the chloride at Ru(II) from $\mathbf{C^1}$ led to cationic intermediate $\mathbf{D^+}$ showing a bidentate acetate ligand and lying at −4.4 [−3.4] [*4.0*] kcal mol^{-1}. Going through $\mathbf{TS(C^1\text{-}D^+)}$, such dissociation required surpassing a ΔG_r of 17.1 [16.4] [*23.7*] kcal mol^{-1}. Nevertheless, $\mathbf{D^+}$ can also be formed by dissociation of acetate from diacetate complex $\mathbf{C^2}$, *via* $\mathbf{TS(C^2\text{-}D^+)}$, which showed a slightly higher ΔG_r of 18.0 [18.4] [*26.7*] kcal mol^{-1} (see ESI, Schemes S4a and S4b†). Alternative reaction pathways to cationic intermediate $\mathbf{D^+}$ by coordination of ligand **A** to cationic precursors $\mathbf{B^+}$ or $\mathbf{B^{+S}}$ resulted in a higher energy by more than 5 kcal mol^{-1} (see ESI, Scheme S4c†).

From $\mathbf{C^2}$, equilibria involving slippage of the *p*-cymene moiety (from η^6- to η^2-ligand) and its decoordination or substitution by solvent or a second imine molecule give rise to key neutral intermediates $\mathbf{F^c}$, **F**, $\mathbf{F^S}$, and $\mathbf{F^A}$ which are found at 6.6, 16.1, 2.9, and −6.1 [8.2, 18.8, 5.8, and −2.8] [*20.3*, *31.5*, *17.9* and *9.4*] kcal mol^{-1}, respectively (see Scheme 4, entry b). Most stable TS structures for the ligand exchange processes at ruthenium were located on the dissociative pathways. Thus, from $\mathbf{F^c}$, decoordination of the *p*-cymene moiety through $\mathbf{TS(F^c\text{-}F)}$ required surpassing a ΔG_r of 18.7 [>26.9] [*>39.3*][46] kcal mol^{-1} and gave rise to the 16-electron species **F**. Addition of a solvent molecule to **F**, *via* $\mathbf{TS(F\text{-}F^S)}$, led to the solvated diacetate complex $\mathbf{F^S}$. The lowest energy pathway for the addition of a second imine molecule to **F** involved coordination of the *N*-phenyl moiety to ruthenium(II), acting as an η^2-ligand, to form the **F·A** complex, followed by rearrangement to the *N*,*N*-coordinated bis-imine ruthenium complex $\mathbf{F^A}$ *via* $\mathbf{TS(F\text{-}F^A)}$ which was characterized by a ΔG_r of 19.5 [19.1] [*30.0*] kcal mol^{-1} (see ESI, Schemes S5a and S5b†). Competing TS structures in the solvent-assisted interchange pathways from $\mathbf{F^c}$ to $\mathbf{F^S}$ or to $\mathbf{F^A}$ were also located but resulted in higher energies (see ESI, Scheme S5c†).

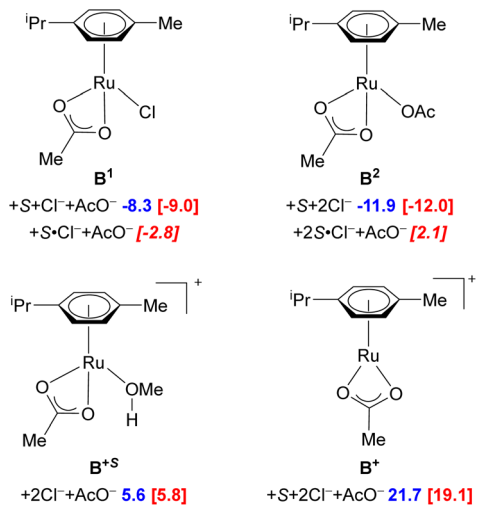

Chart 2 Acetate derivatives from [RuCl$_2$(*p*-cymene)$_2$]$_2$ dimer opening. Relative quasi-harmonic free energies (in kcal mol^{-1}) calculated at the DLPNO-CCSD(T)/CBS(CPCM) level in methanol (298 K, 1 M) using geometries optimized at the M06/cc-pVDZ-PP[Ru](IEF-PCM) level are shown in blue. The corresponding values calculated at the same level by using geometries optimized at the ωB97X-D3/cc-pVDZ-PP[Ru](CPCM) level are shown between brackets in red. Energy values calculated at the DLPNO-CCSD(T)/CBS(SMD) level in methanol (298 K, 1 M) are shown in italics.

2.2. C–H activation events

2.2.1 Pathways involving cationic intermediates. Two reactive conformations could be located for cationic intermediate $\mathbf{D^+}$, both showing one *ortho* C–H bond (at the benzylidene moiety) pointing to the metal atom, and thus, two different reaction pathways for C–H activation were considered (see Scheme 5, entry a). The first pathway departs from conformation $\mathbf{D^+}$, which is characterized by an intramolecular hydrogen bond interaction between the *ortho* C–H benzylidene moiety and the proximal oxygen atom of the bidentate acetate ligand (C–H···O distance of 2.20 [2.23] Å). From $\mathbf{D^+}$ the κ^2–κ^1-displacement of the proximal acetate arm by the incoming C–H bond, *via* six-membered TS structure $\mathbf{\textit{cis}\text{-}TS(D^+\text{-}E^+)1}$, gives rise to the agostic intermediate $\mathbf{\textit{cis}\text{-}INT(D^+\text{-}E^+)}$, which maintains the hydrogen bond interaction (C–H···O distance of 2.05 [2.14] Å). The second pathway starts from $\mathbf{D^{+}\star}$, located −1.8 [−1.7] [*1.8*] kcal mol^{-1} away from $\mathbf{D^+}$, which also undergoes dis-

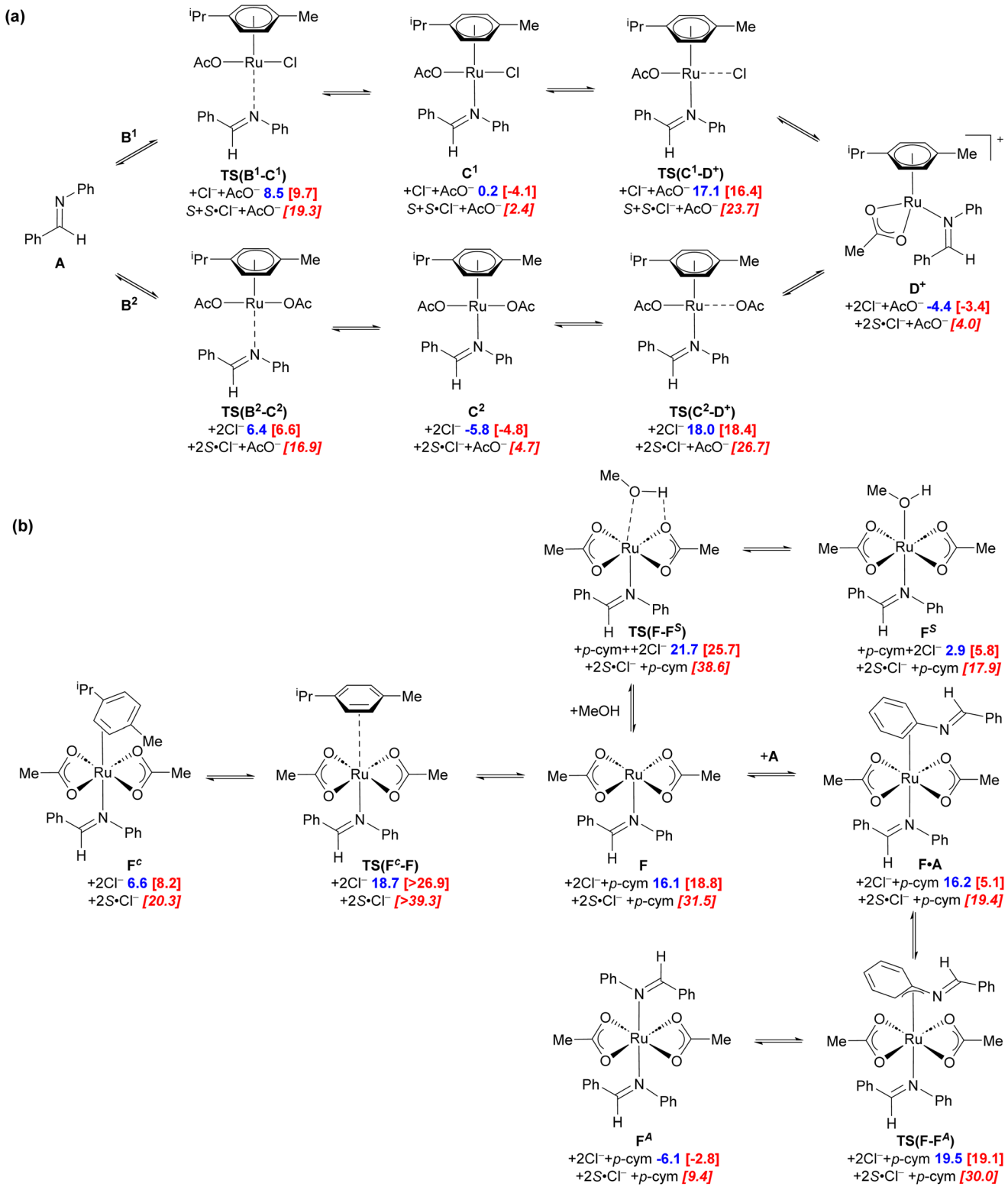

Scheme 4 (a) Formation of cationic intermediate D^+ by the reaction of imine (**A**) with monomeric precursors B^1 or B^2 followed by anion dissociation; (b) equilibria between diacetate complex C^2 and neutral intermediates of the F^L series by *p*-cymene slippage or decoordination and substitution by solvent or a second imine molecule. Relative quasi-harmonic free energies (in kcal mol^{-1}) calculated at the DLPNO-CCSD(T)/CBS(CPCM) level in methanol (298 K, 1 M) using geometries optimized at M06/cc-pVDZ-PP[Ru](IEF-PCM) are shown in blue. The corresponding values calculated at the same level by using geometries optimized at the ωB97X-D3/cc-pVDZ-PP[Ru](CPCM) level are shown between brackets in red. Energy values calculated at the DLPNO-CCSD(T)/CBS(SMD) level in methanol (298 K, 1 M) are shown in italics.

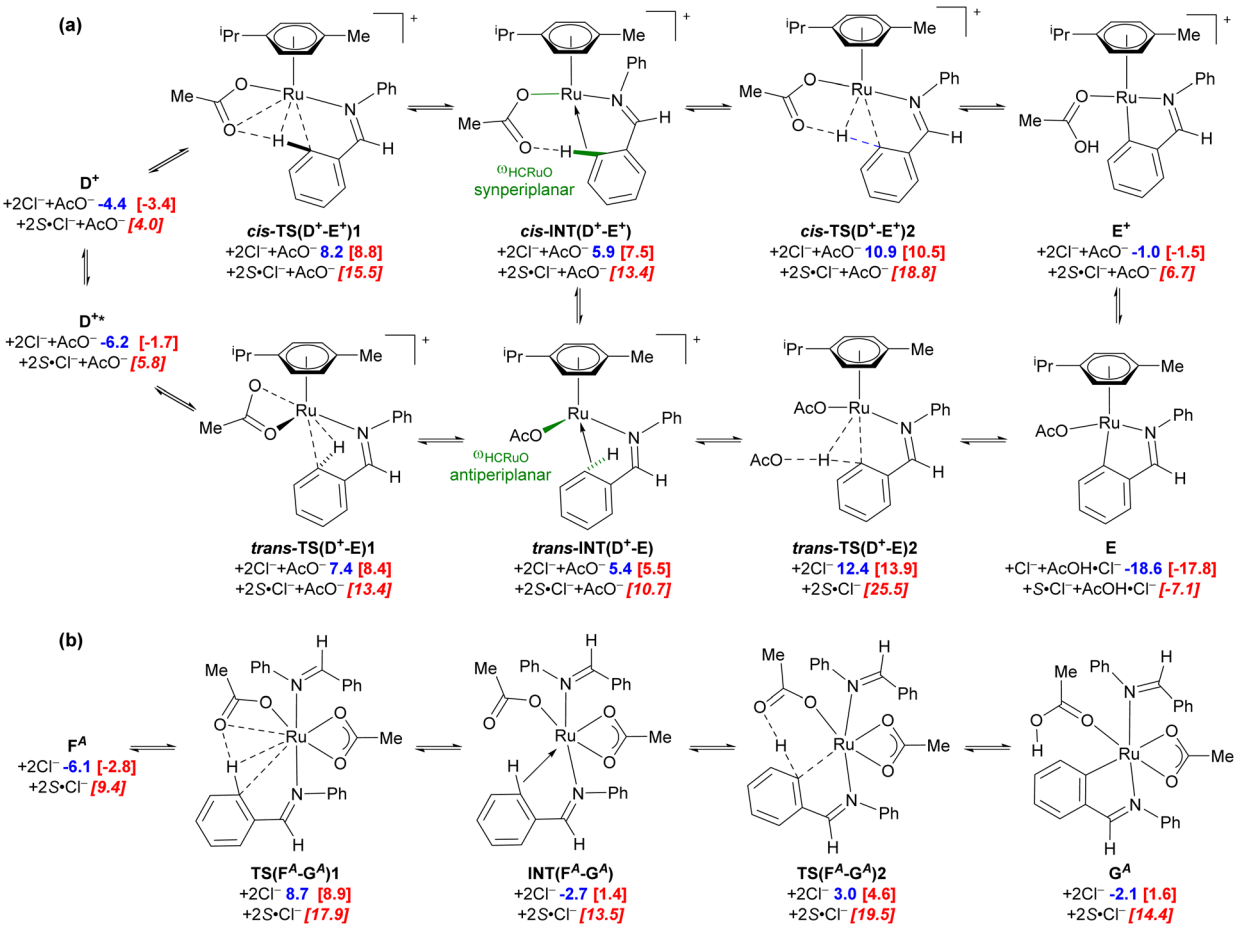

Scheme 5 (a) C–H activation of the cationic precursor (D^+ or D^{+*}), involving the cationic agostic intermediates (***cis*-INT(D^+-E^+)** or ***trans*-INT(D^+-E)**) and intramolecular or intermolecular routes for proton abstraction and formation of the acetate–ruthenacycles (E^+ and **E**). (b) C–H activation of the bis-imine diacetate neutral intermediate F^A, involving the agostic intermediate **INT(F^A-G^A)** and intramolecular proton abstraction leading to ruthenacycle G^A. Relative quasi-harmonic free energies (in kcal mol^{-1}) calculated at the DLPNO-CCSD(T)/CBS(CPCM) level in methanol (298 K, 1 M) using the geometries optimized at M06/cc-pVDZ-PP[Ru](IEF-PCM) are shown in blue. The corresponding values calculated at the same level by using the geometries optimized at the ωB97X-D3/cc-pVDZ-PP[Ru](CPCM) level are shown between brackets in red. Energy values calculated at the DLPNO-CCSD(T)/CBS(SMD) level in methanol (298 K, 1 M) are shown in italics.

placement of the distal acetate arm by the incoming C–H bond and leads to competing intermediate ***trans*-INT(D^+-E)**. This intermediate shows a strong agostic interaction that develops *trans* to the acetate ligand (C–H and Ru–O bonds are close to an antiperiplanar disposition) and was calculated to be 0.5 [2.0] [*2.7*] kcal mol^{-1} lower in energy than its *cis* counterpart. Going through TS structure ***trans*-TS(D^+-E)1** the second reaction pathway must overcome a ΔG_r of 7.4 [8.4] [*13.4*] kcal mol^{-1} and thus is favoured over that involving ***cis*-TS(D^+-E^+)1** by 0.8 [0.4] [*2.1*] kcal mol^{-1}. Related agostic intermediates have been characterized in previous computational works on acetate-assisted cycloruthenation but, to the best of our knowledge, this is the first time a *trans* relationship between the activated C–H bond and the coordinated acetate has been reported.[47]

Two different pathways for the acetate-assisted C–H activation event have been considered, involving deprotonation of the cationic agostic intermediates by either a complexed acetate or a free one, as depicted in Scheme 5(a). Both deprotonation pathways, denoted as intramolecular and intermolecular, respectively, may lead to the same acetate–ruthenacycle **E** after a molecule of acetic acid is released. In the intramolecular pathway, starting from ***cis*-INT(D^+-E^+)**, the κ^1-acetate ligand abstracts the proton using the unbonded oxygen atom and gives rise to cationic intermediate E^+, which was found at −1.0 [−1.5] [*6.7*] kcal mol^{-1}. The intramolecular pathway involves the classical AMLA/CMD process, which, going through the six-membered cyclic TS structure ***cis*-TS(D^+-E^+)2**, must overcome a ΔG_r of 10.9 [10.5] [*18.8*] kcal mol^{-1}. Alternatively, the association of a free molecule of acetate to the activated C–H bond in ***trans*-INT(D^+-E)** facilitates subsequent intermolecular deprotonation leading to intermediate **E** and HOAc. After the association of HOAc with chloride to form $AcOH{\cdot}Cl^-$, the acetate–ruthenacycle **E** was calculated to be 18.6 [17.8] [*7.1*] kcal mol^{-1} more stable than the starting compounds. Going through TS structure ***trans*-TS(D^+-E)2** inter-

molecular deprotonation (also denoted as the external-CMD pathway) required surpassing a ΔG_r of 12.4 [13.9] [*25.5*] kcal mol^{-1} and was disfavoured over the intramolecular one by 1.5 [3.4] [*6.7*] kcal mol^{-1}.[48]

2.2.2 Pathways involving neutral intermediates. We next studied the C–H activation event from the neutral diacetate precursors of the $\mathbf{F^L}$ series. Calculations indicate that cyclometallation of the neutral 18-electron derivatives $\mathbf{F^c}$, $\mathbf{F^S}$, $\mathbf{F^{2S}}$ and $\mathbf{F^A}$ (with a *p*-cymene moiety, one or two solvent molecules or a second substrate molecule acting as η^2-ligands, respectively) also takes place in two consecutive steps with the participation of an agostic intermediate. The lowest energy pathway for the C–H activation event on the neutral intermediates departs from the bis-imine diacetate complex $\mathbf{F^A}$ (see Scheme 5, entry b). κ^2–κ^1-Displacement of one acetate arm in $\mathbf{F^A}$ takes place easily through the six-membered TS structure $\mathbf{TS(F^A\text{-}G^A)1}$, found at 8.7 [8.9] [*17.9*] kcal mol^{-1}, and gives rise to agostic intermediate $\mathbf{INT(F^A\text{-}G^A)}$. From this intermediate, intramolecular deprotonation *via* AMLA/CMD TS structure $\mathbf{TS(F^A\text{-}G^A)2}$ requires overcoming a ΔG_r of 3.0 [4.6] [*19.5*] kcal mol^{-1} and gives rise to bis-imine cycloruthenate $\mathbf{G^A}$, found at −2.1 [1.6] [*14.4*] kcal mol^{-1}.[49] An equilibrium between cycloruthenate intermediates $\mathbf{G^A}$ and **E**, involving departure of HOAc and one imine molecule as well as coordination of the *p*-cymene moiety as a η^6-ligand at ruthenium have not been studied in detail, but were calculated to be exergonic by more than 12 [17] [*21*] kcal mol^{-1} and should also take place easily. Analogous C–H activation processes starting from neutral intermediates $\mathbf{F^c}$, $\mathbf{F^S}$ or $\mathbf{F^{2S}}$ (with the *p*-cymene moiety or one or two solvent molecules acting as a η^2-ligands) required overcoming energy barriers more than 10 kcal mol^{-1} higher in energy than that calculated for the involvement of $\mathbf{F^A}$. Separate schemes for each of these reaction channels are included in the ESI (see Schemes S7, S8 and S9†).

2.3. Final ligand exchange processes at ruthenacycles

Cyclometallated chloro(*p*-cymene)Ru(II) complexes have interesting biological[6p–r] and catalytic[6c,d,e,f] activities. The replacement of the chloride leaving group by a water molecule is thought to be essential for their mechanism of action in biological systems, while the chloro/carboxylate ligand exchange processes are mandatory for their entrance into the catalytic cycles of carboxylate-assisted C–H bond functionalizations. As neither the detailed mechanism nor the kinetic relevance of the chloro/carboxylate ligand exchange processes at cyclometallated (*p*-cymene)Ru(II) complexes are yet clear, we decided to undertake modelling in methanol solution by using the acetate cycloruthenate **E** as a model system. At our benchmark level, the lowest energy route from **E** to chloro cycloruthenate **H** follows an associative pathway with solvent assistance, as depicted in Scheme 6. Initial acetate/methanol exchange at ruthenium through TS structure $\mathbf{TS(E\text{-}H)1}$·***S*** required surpassing a ΔG_r of 9.3 [10.7] [*21.4*] kcal mol^{-1} and led to the monosolvated intermediate $\mathbf{INT(E\text{-}H)^+}$·***S*** (see ESI, Scheme S10a†). Subsequent methanol/chloride exchange on the cationic intermediate takes place through $\mathbf{TS(E\text{-}H)2}$·***S*** (ΔG_r of 8.8 [9.5] [*17.4*] kcal mol^{-1}) to afford the chloro cycloruthenate **H** (see ESI, Scheme S10b†), which was found to be 19.3 [18.3] [*10.6*] kcal mol^{-1} lower in energy than the starting compounds. Thus, final acetate/chloride exchange on the ruthenacycle is calculated to be exergonic by 0.7 [0.5] [*3.5*] kcal mol^{-1}. Dissociative pathways for the acetate/chloride exchange, with or without solvent assistance, and direct acetic acid/chloride exchange on intermediate $\mathbf{E^+}$ were also considered but were more than 4 kcal mol^{-1} higher in energy (see ESI, Scheme S10c†).

2.4. Competence between reaction pathways

2.4.1 Energy profiles using the CPCM solvation model

2.4.1.1. Standard gas-phase thermochemical analysis. 3D representations[50] of the optimized geometries and energy plots at the DLPNO-CCSD(T)/CBS(CPCM) level for the most significant stationary points located on the competitive pathways are shown in Fig. 1. Fig. 1(a) plots the energy results evaluated under standard conditions (1.0 M) after geometry optimizations (in methanol solution) with the M06 functional. The corresponding plot calculated at the same level by using the ωB97X-D3 geometries is included in the ESI,† see Fig. S2(a).† In these plots, relative energies for the pre-activation and C–H activation processes (from $\mathbf{B^1}$ to **E**) are referenced to $\mathbf{A}+\frac{1}{2}\mathbf{B^0}$ + 2AcO$^-$ while for the final ligand exchange processes on the

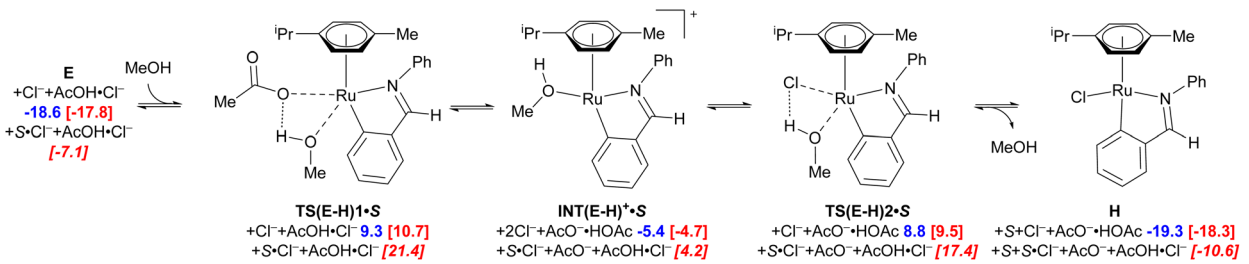

Scheme 6 Acetate/chloride exchange and formation of the chloro–ruthenacycle (**H**). Relative quasi-harmonic free energies (in kcal mol^{-1}) calculated at the DLPNO-CCSD(T)/CBS(CPCM) level in methanol (298 K, 1 M) using the geometries optimized at M06/cc-pVDZ-PP[Ru](IEF-PCM) are shown in blue. The corresponding values calculated at the same level by using the geometries optimized at the ωB97X-D3/cc-pVDZ-PP[Ru](CPCM) level are shown between brackets in red. Energy values calculated at the DLPNO-CCSD(T)/CBS(SMD) level in methanol (298 K, 1 M) are shown in italics. Hydrogen bonds are represented by dotted lines.

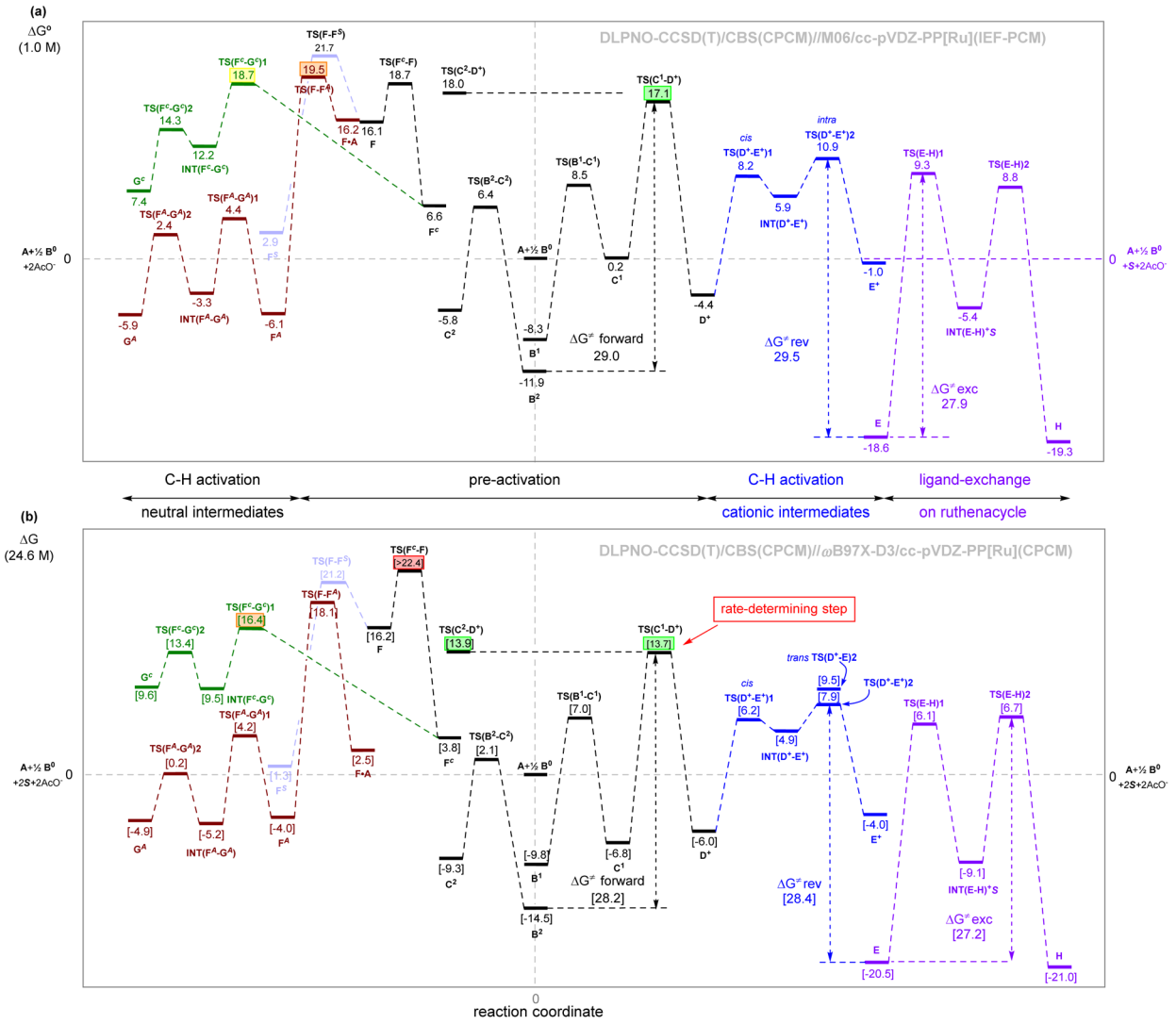

Fig. 1 Relative quasi-harmonic Gibbs energy plots calculated at the DLPNO-CCSD(T)/CBS(CPCM) level in methanol (in kcal mol^{-1}). (a) At 298 K and 1 M after geometry optimizations at the M06/cc-pVDZ-PP[Ru](IEF-PCM) level. (b) At 298 K and 24.6 M after geometry optimizations at the ωB97X-D3/cc-pVDZ-PP[Ru](CPCM) level. Pre-activation by anion dissociation and ligand exchange processes at ruthenium are shown in black, C–H activations involving cationic intermediates are shown towards the right in blue and the corresponding processes involving neutral intermediates are shown towards the left in brown and green. The final ligand exchange processes at ruthenacycles are shown towards the right in purple.

ruthenacycle (from **E** to **H**) **A** + $\frac{1}{2}$**B⁰** + ***S*** + 2AcO$^-$ is set to zero. Analysis of both plots allows us to conclude the following. First, chemical equilibria between chloro and acetate ruthenium(*p*-cymene) precursors are shifted towards monomeric diacetate complex **B²**, which constitutes the lowest energy point of the profiles and serves as the reference for calculating the barrier heights in the forward reaction. From **B²** (located in Fig. 1 under the precursors **A** + $\frac{1}{2}$**B⁰**, which serve as the reference for the reaction coordinate) the lowest energy pathway to cycloruthenates involves cationic intermediates **D⁺**, **INT(D⁺-E⁺)** and **E⁺**. In this pathway the imine/chloride ligand exchange process on ruthenium leading to key cationic intermediate **D⁺** constitutes the slower, RDS for the global process. Thus, an activation energy of 29.0 [28.4] kcal mol^{-1} is calculated for the forward reaction. Subsequent steps from cationic intermediate **D⁺** to acetate–cycloruthenate **E** are faster, as the CMD/AMLA C–H activation must surpass a barrier of 22.8 [22.5] kcal mol^{-1}. Formation of acetate–cycloruthenate **E** from precursor **B²** is found to be exergonic by 6.7 [5.8] kcal mol^{-1}. The final solvent-assisted chloride/acetate ligand exchange on ruthenacycle **E** must overcome an activation free energy of 27.9 [28.5] kcal mol^{-1} and should take place faster than [or at comparable rate to] anion dissociation leading to key cationic intermediate **D⁺**. Formation of chloro–ruthenacycle **H** from acetate precursor **E** is calculated to be exergonic by only 0.7 [0.5] kcal mol^{-1} and may constitute an equilibrium process, which is mainly driven by dissociation of AcOH·Cl$^-$ and formation of AcOH·AcO$^-$ (see ESI, Scheme S11†). As the energy barrier for the forward reaction (29.0 [28.4] kcal mol^{-1} *via* **TS(C¹-D⁺)**) is almost the same as the barrier required for the reversion of cyclometallation

(from **E** to $\mathbf{D}^+$ through ***cis*-TS($\mathbf{D}^+$-$\mathbf{E}^+$)2**, 29.5 [28.3] kcal mol^{-1}), calculations show that the cyclometallation of benzaldimines in methanol should be reversible, as previously reported for ruthenium-catalyzed hydroarylation[7e] or deuteration[7h] of aromatic carbonyl compounds using imines as TDGs in apolar solvents and also in accordance with deuterium exchange experiments reported for many C–H bond ruthenations of related arenes equipped with *N*-containing DGs in polar protic solvents such as water, methanol, acetic acid or HFIP.[51]

On the basis of the results obtained at the DLPNO-CCSD(T)/CBS(CPCM) level, participation of the reaction pathways involving neutral intermediates should be excluded. Neutral intermediates are shown in Fig. 1 towards the left of the $\mathbf{A}+\frac{1}{2}\mathbf{B}^{\mathbf{0}}$ reference. From $\mathbf{F}^{\mathbf{c}}$, the neutral intermediate with the *p*-cymene moiety acting as the η^2-ligand, the slowest step corresponds to the formation of agostic intermediate **INT($\mathbf{F}^{\mathbf{c}}$-$\mathbf{G}^{\mathbf{c}}$)** *via* TS structure **TS($\mathbf{F}^{\mathbf{c}}$-$\mathbf{G}^{\mathbf{c}}$)1**. Thus, the progress of the C–H activation event through the pathway involving neutral intermediate $\mathbf{F}^{\mathbf{c}}$ will show an activation energy of 30.6 [32.9] kcal mol^{-1}, 1.6 [4.5] kcal mol^{-1} higher than that offered by the pathway involving cationic intermediate $\mathbf{D}^+$. Alternative reaction pathways involving solvated or bis-imine ligated neutral intermediates ($\mathbf{F}^{\mathbf{S}}$ and $\mathbf{F}^{\mathbf{A}}$) are also precluded due to higher activation energies for the exchange processes of the *p*-cymene ligand with methanol or a second imine molecule. Nevertheless, in a related fashion to that reported by Ackermann *et al.* on the grounds of their computational investigation of the acetate-assisted ruthenium-catalyzed C–H activations of one of two *N*-coordinated arylpyridine motifs,[33c] the bis-imine *N*-ligated ruthenium intermediates $\mathbf{F}^{\mathbf{A}}$, **INT($\mathbf{F}^{\mathbf{A}}$-$\mathbf{G}^{\mathbf{A}}$)** and $\mathbf{G}^{\mathbf{A}}$ could offer the lowest energy pathway for the cyclometalation of benzaldimines in apolar solvents at higher reaction temperatures or at room temperature under visible-light irradiation conditions, which are known to facilitate decomplexation of the *p*-cymene ligand from the neutral ruthenium intermediates.[52] For the system under study the energy barrier required for C–H activation *via* the neutral bis-imine ligated intermediate **INT($\mathbf{F}^{\mathbf{A}}$-$\mathbf{G}^{\mathbf{A}}$)** was calculated to be *ca.* 2 [2] kcal mol^{-1} lower than the corresponding barrier in the pathway involving the cationic intermediate ***cis*-INT($\mathbf{D}^+$-$\mathbf{E}^+$)**.

A comparison of the energy plots obtained by performing the geometry optimizations with the M06 or ωB97X-D3 functionals (Fig. 1(a) and Fig. S2(a),† respectively) reveals only small differences. Activation energies calculated at the DLPNO-CCSD(T)/CBS(CPCM) level for the geometries optimized with the ωB97X-D3 functional for anion dissociation and formation of key cationic intermediate $\mathbf{D}^+$, the C–H activation event from $\mathbf{D}^+$ to $\mathbf{E}^+$ and the final solvent-assisted dissociative ligand exchange at ruthenacycles differs by less than 1 kcal mol^{-1} from the corresponding values obtained by using the M06 geometries. Nevertheless, for the competing pathways involving neutral intermediates **F–G** the calculated activation energies were found to be between 2 and 9 kcal mol^{-1} higher when the geometry optimizations were performed with the ωB97X-D3 functional instead of the M06 one. Thus, inclusion of dispersion energy corrections and range-separated treatment for the exchange contributions in the DFT geometry optimizations appears to improve the discrimination between the pathways involving the cationic and neutral intermediates.

2.4.1.2. Condensed-phase thermochemical analysis. Since entropic contributions calculated within the ideal gas approximation at 1.0 M are likely to exaggerate the expected values in the condensed phase, a second thermochemical analysis was performed to model the reduction of the translational degrees of freedom at the concentration of the liquid solvent. When a pressure parameter to adjust the concentration to that of the liquid solvent[53] (24.6 M for methanol) is taken into consideration, monosolvation of chloride anions, association of chloride to acetic acid and the formation of hydrogen diacetate (by association of acetate to acetic acid) are more favoured processes (by an additional term of *ca.* 1.9 [1.9] kcal mol^{-1}), as depicted in Scheme S11 of the ESI.† Relative quasi-harmonic Gibbs energies calculated at the DLPNO-CCSD(T)/CBS(CPCM) level in the condensed phase (298 K, 24.6 M) using geometries optimized at the ωB97X-D3/cc-pVDZ-PP[Ru](CPCM) level for the most significant stationary points are depicted in Fig. 1(b). Due to the exergonic monosolvation of the chloride anions under condensed-phase conditions, in Fig. 1(b) the relative energies are referenced to $\mathbf{A} + \frac{1}{2}\mathbf{B}^{\mathbf{0}} + 2\boldsymbol{S} + 2\mathrm{AcO}^-$.

By comparison of Fig. 1(b) and Fig. S2(a) in the ESI† some differences can be observed for the progress of cyclometallation in the condensed phase with respect to standard conditions. (1) In the forward direction the Gibbs energies of activation remain unchanged for the formation of key intermediate $\mathbf{D}^+$ and for the subsequent C–H activation involving cationic intermediates (at *ca.* [28] and [22] kcal mol^{-1}, respectively) but are reduced for the final ligand exchange process at cycloruthenates (by *ca.* [1] kcal mol^{-1}); (2) the energy barrier for C–H activation in the reverse direction (from **E** to $\mathbf{D}^+$) is also conserved at *ca.* [28] kcal mol^{-1}. Thus, under condensed-phase conditions the pathway involving cationic intermediates also offers the lowest energy profile and the reversibility of the C–H activation event should not be compromised. It should be noted that the solvent compression effect significantly reduces the energy gap between **TS($\mathbf{C}^1$-$\mathbf{D}^+$)** and **TS($\mathbf{C}^2$-$\mathbf{D}^+$)** and between ***cis*-TS($\mathbf{D}^+$-$\mathbf{E}^+$)2** and ***trans*-TS($\mathbf{D}^+$-E)2** (by *ca.* [1.9] kcal mol^{-1}). Thus, the contribution of the pathways involving acetate anion dissociation in the RDS or intermolecular deprotonation for the C–H activation event may be increased in polar protic solvents.[48] The same conclusions can be drawn by comparing the energy plots calculated under standard and condensed-phase conditions by using the M06 geometries (depicted in Fig. 1(a) and Fig. S2(b) in the ESI†).

2.4.1.3. Performance of DFT methods. Single point energy evaluations with top hybrid DFT performers in the MOR41 and MOBH35 databases[37] using an augmented polarized triple-ζ basis set (denoted as aug-cc-pVTZ-PP[Ru], see Computational methods in the ESI† for further details) did not allow to reproduce the DLPNO-CCSD(T)/CBS(CPCM) energy results (see Table S2 in the ESI†). In a different manner, single point energy evaluations with double-hybrid DFT methods were found to be in good agreement with our

benchmark calculations at the DLPNO-CCSD(T)/CBS(CPCM) level. According to the results obtained with the B2GP-PLYP,[54] B2K-PLYP[55] or PWPB95[56] methods, the formation of key cationic intermediate $\mathbf{D}^+$ was the RDS and the reaction channels involving neutral intermediates were all disfavoured by more than 5 [3] kcal mol^{-1}. Nevertheless, energy evaluations with double-hybrid DFT methods underestimated the exergonic character of the global transformation by more than 3 [2] kcal mol^{-1} and overestimated the Gibbs activation energy for the RDS by more than 9 [4] kcal mol^{-1}. Better correlation with our benchmark results was obtained by applying Grimme's D3 (BJ)[57] or D4[58] dispersion energy corrections to the energy evaluations with the PWPB95 method, as the overestimation of the activation energies was reduced to 3 [2] kcal mol^{-1}. Moreover, the lowest MUEs for the relative Gibbs energies of precursors and cyclometallated intermediates ($\mathbf{B^1}$, $\mathbf{B^2}$, **E** and **H**) and for the whole set of barrier heights in Table S2† were obtained when the energy evaluations were performed with the PWPB95 method adding the D3(BJ) or D4 dispersion energy corrections and using the ωB97X-D3 geometries (see entries 5 and 20). In addition, by using this computational scheme (PWPB95 + D3(BJ)//ωB97X-D3) the MUE for the barrier heights along the most favourable pathway and involving the cationic intermediates was only 0.3 kcal mol^{-1} (see entry 21).

2.4.2 Energy profiles using the SMD solvation model

2.4.2.1. Pure implicit (SMD) solvation model. As the SMD model provides a more realistic description of the non-electrostatic solute–solvent interactions and is recommended for the estimation of the solvation energies of charged species, following the suggestion of one referee, we have performed energy evaluations by employing the SMD model for the most significant stationary points located after geometry optimizations with the ωB97X-D3 functional. At our benchmark level with the SMD solvation model, monosolvation of chloride anions and their association to acetic acid are favoured processes (by −1 and −2 kcal mol^{-1}, respectively), while the formation of hydrogen diacetate is disfavoured (by 2 kcal mol^{-1}), even under standard conditions (see Scheme S11 of the ESI†). Thus, using the SMD solvation model, to describe the most stable aggregation states and relative energies for all the intermediates represented in Schemes 4–6, the chloride anions have been replaced by those that are monosolvated or associated with acetic acid. Plots of the energy results at the DLPNO-CCSD(T)/CBS(SMD) level evaluated under standard conditions (1.0 M) and under condensed-phase conditions (24.6 M) are included in the ESI† (see parts (a) and (b) of Fig. S3†). According to these SMD profiles (1) the chemical equilibria between chloro and acetate ruthenium(*p*-cymene) precursors are shifted towards monomeric diacetate complex $\mathbf{B^1}$, which sets the reference for calculating the barrier height for cycloruthenation in the forward direction; (2) the lowest energy pathway for C–H bond activation also involves cationic intermediates, (3) an activation energy of [26.9] kcal mol^{-1} is calculated for chloride dissociation leading to cationic intermediate $\mathbf{D}^+$, (4) subsequent CMD/AMLA C–H activation events from $\mathbf{D}^+$ to $\mathbf{E}^+$ are faster and require an activation energy of [21.2] kcal mol^{-1}, (5) formation of the acetate–cycloruthenate **E** from precursor $\mathbf{B^1}$ is found to be exergonic by [4.7] kcal mol^{-1} and (6) the C–H activation event is reversible and must surpass an activation barrier of [25.9] kcal mol^{-1} in the reverse direction (from **E** to $\mathbf{D}^+$). Finally, according to the SMD profile, the progress of C–H bond activation through the pathways involving neutral diacetate ruthenium intermediates is also precluded in methanol as solvent, as it would require activation energies more than [9] kcal mol^{-1} higher than that offered by the pathway involving cationic intermediate $\mathbf{D}^+$.

Analysis of the energy plots calculated at the benchmark level with the SMD model under standard conditions and condensed-phase conditions (see parts (a) and (b) of Fig. S3 in the ESI†) reveals some differences and similarities to those aspects described above for the CPCM profiles. The switch from standard to condensed-phase conditions in the SMD profiles (a) reduces the energy barriers for anion dissociation leading to key intermediate $\mathbf{D}^+$ and for subsequent C–H activation involving cationic intermediate $\mathbf{INT(D^+\text{-}E^+)}$ by 1.9 kcal mol^{-1} (from [26.9] to [25.0] and from [21.2] to [19.3] kcal mol^{-1}, respectively), while the energy barrier for the reverse reaction (from **E** to $\mathbf{D}^+$) is maintained (at ca. [26] kcal mol^{-1}); (b) the energy gap between $\mathbf{TS(C^1\text{-}D^+)}$ and $\mathbf{TS(C^2\text{-}D^+)}$ and between ***cis*-TS(D$^+$-E$^+$)2** and ***trans*-TS(D$^+$-E)2** is also reduced by *ca.* [1.8] kcal mol^{-1}.

In this manner, energy plots calculated for our benchmark level using either the SMD or CPCM solvation models describe the C–H bond activation of benzaldimine in MeOH as a reversible and kinetically irrelevant process. Nevertheless, a remarkable difference of 1.5/3.2 kcal mol^{-1} is observed for the activation energies leading to cycloruthenate formation, as the values calculated using the CPCM model under standard and condensed-phase conditions are [28.4] and [28.2] kcal mol^{-1} and are reduced to [26.9] and [25.0] kcal mol^{-1} with the use of the SMD model. All these values are in line with the activation energies reported in previous computational studies on the C–H bond activation processes for related arenes equipped with heterocyclic DGs in alcoholic solvents, which have been described as system-dependent and generally ranging from 25 to 28 kcal mol^{-1}.[5g,18,19,23e,29a,b]

2.4.2.2. Hybrid explicit–implicit (SMD) solvation model. Continuum solvation models are computationally efficient and are widely used in computational homogeneous catalysis. In particular, PCM and SMD solvation models have been successfully employed to investigate many ruthenium(II)-catalyzed C–H activation and functionalization processes in almost all kinds of solvents (as 2-MeTHF, dioxane, toluene, DCE, acetonitrile, MeOH, TFE, *tert*-butanol, HFIP, or AcOH).[12–33] Nevertheless, the suitability of implicit solvent models for the study of ionic reactions that are performed in protic solvents is still controversial, as strong, specific, solvent–solute H-bonding interactions are seemingly ignored. These kinds of directed interactions are not captured by the CPCM and SMD models and this deficiency could compromise the accuracy of our results. To overcome these limitations, we considered the application of a hybrid explicit–implicit (cluster/continuum) solvation model,[42] by adding a limited number of solvent

molecules to the reaction system inside the continuum model cavity. Nevertheless, it is not clear how many solvent molecules need to be added to describe the solvent effects with the desired accuracy, while the addition of solvent molecules to selected binding sites or regions around the solute is guided by assumptions and may change from one intermediate to another along the reaction coordinate. In any case, the static *ab initio* evaluation of a small set of low-lying configurations for the solvent–solute clusters can lead to meaningful improvements in the description of the "averaged" solvent effects by pure implicit solvation models, thus providing insights into the relevance of the solvent–solute H-bonding interactions and more "realistic" energetic estimations.

Taking into consideration experimental measurements and the results of molecular dynamics simulations that are consistent with a coordination shell of chloride or acetate anions in methanol solutions essentially made up to 3 or 4 solvent molecules,[59] and trying to get a glance of the relevance of specific solvent–solute interactions in the acetate-assisted C–H activation of benzaldimine at $[RuCl_2(p\text{-cymene})]_2$ in MeOH, we studied the addition of up to 3 or 4 explicit MeOH molecules to the most relevant stationary points in the C–H bond activation pathway involving cationic intermediates, from $\mathbf{B^1}$ to $\mathbf{E^+}$. We considered it reasonable to assume that one, two or three solvent molecules should hydrogen bond to the chloride and acetate moieties. After geometry optimizations at the ωB97X-D3/cc-pVDZ-PP[Ru](CPCM) level in methanol solution, the relative quasi-harmonic Gibbs energies of the solvated species were evaluated at our benchmark level (DLPNO-CCSD(T)/CBS(SMD)) using separate reagents ($\mathbf{A} + \frac{1}{2}\mathbf{B^0} + 2AcO^-$) and an adequate number of explicit solvent molecules (to ensure the stoichiometric balance) as a common energetic reference. As described below (in the energy profile using the SMD solvation model) for the non-solvated reaction channel, aside from the MeOH molecules maintaining specific interactions near the reaction center, one explicit MeOH molecule is needed to accomplish the exergonic monosolvation of the chloride that is freed through the formation of the $\mathbf{B^1}$ precursors. Thus, in Fig. 2 (and in Fig. S4, S5 and S6 of the ESI†) the active MeOH molecules (surrounding the reaction center of any intermediate or TS) are highlighted in yellow while the solvent molecule associated with the stoichiometric chloride is highlighted in blue. The non-solvated and solvated reaction channels, considering specific interactions of any intermediate with zero, one, two or three (yellowish) MeOH molecules, are denoted as the S_0-, S_1-, S_2- and S_3-reaction channels, respectively. The (yellowish) methanol molecules bound the chloride atoms are denoted as $\boldsymbol{S}$, and those associated with the acetate moiety by H-bonding the oxygen atom bound to ruthenium(II) or one in the pendant free arm are denoted as $\boldsymbol{S^k}$ and $\boldsymbol{S^p}$, respectively. Solvent molecules bound to an external acetate are designated as $\boldsymbol{S^e}$ and those involved in proton-relay mechanisms are designated as $\boldsymbol{S^r}$.

Based on the results described in previous sections, we focused our analysis of the specific solvent–solute interactions in chloride dissociation from intermediates $\mathbf{C^1}\cdot\boldsymbol{S_n}$ leading to $\mathbf{D^+}$ *via* $\mathbf{TS(C^1\text{-}D^+)}\cdot\boldsymbol{S_n}$ and C–H bond activation process from $\mathbf{D^+}$ to cycloruthenate $\mathbf{E^+}$ *via* $\mathbf{TS(D^+\text{-}E^+)1}\cdot\boldsymbol{S_n}$, $\mathbf{INT(D^+\text{-}E^+)1}\cdot\boldsymbol{S_n}$ and $\mathbf{TS(D^+\text{-}E^+)2}\cdot\boldsymbol{S_n}$. 3D representations of the most significant stationary points located in the S_0-, S_1-, S_2- and S_3-reaction channels are depicted in Fig. 2, including selected distances and relative energies. The complete energy profiles for the S_1-, S_2- and S_3-reaction channels are included in the ESI,† see Fig. S4, S5 and S6,† respectively.

Most stable TS structures located in the S_1-, S_2- and S_3-reaction channels leading to cationic intermediate $\mathbf{D^+}$ showed the chloride leaving group associated with one, two and three MeOH molecules, respectively, with distances and angles falling in the ranges usually chosen to characterize hydrogen bonds (r(H···Cl) < 2.2 Å, r(O···Cl) < 3.2 Å, and θ(OH···Cl) < 14°). The solvated TS structures $\mathbf{TS(C^1\text{-}D^+)}\cdot\boldsymbol{S_n}$ were also characterized by slightly shorter distances between ruthenium and chloride (*ca.* 3.50 A) than the non-solvated one (*ca.* 3.70), indicating a higher early character of these TS structures in the solvated reaction channels. TS structures $\mathbf{TS(C^1\text{-}D^+)}\cdot\boldsymbol{S_1}$, $\mathbf{TS(C^1\text{-}D^+)}\cdot\boldsymbol{S_2}$ and $\mathbf{TS(C^1\text{-}D^+)}\cdot\boldsymbol{S_3}$ were characterized at 30.8, 35.1 and 41.3 kcal mol^{-1}, respectively, showing activation energies of 26.5, 25.9 and 21.5 kcal mol^{-1} relative to the corresponding $\mathbf{B^1}\cdot\boldsymbol{S_1}$, $\mathbf{B^1}\cdot\boldsymbol{S_2}$ and $\mathbf{B^1}\cdot\boldsymbol{S_3}$ precursors (see parts (a) and (b) of Fig. 2 and Schemes S12 and S13a–c in the ESI†). Thus, mono-, di- and tri-solvation of the chloride leaving group in $\mathbf{TS(C^1\text{-}D^+)}\cdot\boldsymbol{S_n}$ led to reductions of 1.0, 3.1 and 5.4 kcal mol^{-1} in the calculated energy barriers from the value of 26.9 kcal mol^{-1} previously estimated for the S_0-reaction channel, *via* $\mathbf{TS(C^1\text{-}D^+)}$. Alternative transition structures for the chloride dissociation step in the S_2- and S_3-reaction channels, showing one MeOH molecule bound to the oxygen atom of the pendant free arm of the acetate moiety were found to be higher in energy (see $\mathbf{TS(C^1\text{-}D^+)}\cdot\boldsymbol{S_2^p}$ and $\mathbf{TS(C^1\text{-}D^+)}\cdot\boldsymbol{S_3^p}$ in Fig. S5, S6 and S13c in the ESI†).

For the analysis of the C–H activation process we found it reasonable to include in the corresponding S_n-reaction channels all possible intermediates and transition states with "n" (yellowish) MeOH molecules, either H-bonding to chloride that was freed during their formation ($Cl^-\cdot\boldsymbol{S_n}$) or bound to the oxygen atoms of the acetate moieties (in $\mathbf{TS(D^+\text{-}E^+)1}\cdot\boldsymbol{S_{(3-n)}}$, $\mathbf{INT(D^+\text{-}E^+)}\cdot\boldsymbol{S_{(3-n)}}$ and $\mathbf{TS(D^+\text{-}E^+)2}\cdot\boldsymbol{S_{(3-n)}}$). In this manner, the lowest energy pathways for C–H bond activation in the S_1-, S_2- or S_3-reaction channels involve the non-solvated TS structures ***cis*-TS(D$^+$-E$^+$)1** and ***cis*-TS(D$^+$-E$^+$)2** accompanied by the corresponding mono-, di- or tri-solvated chloride anions ($Cl^-\cdot\boldsymbol{S}$, $Cl^-\cdot\boldsymbol{S_2}$ or $Cl^-\cdot\boldsymbol{S_3}$, see Fig. 2(c)). Reaction partners ***cis*-TS(D$^+$-E$^+$)1** and ***cis*-TS(D$^+$-E$^+$)2** plus $Cl^-\cdot\boldsymbol{S}$ were found at 15.5 and 18.8 kcal mol^{-1}, respectively, in the S_1-reaction channel, while for the S_2- and the S_3-reaction channels the same TS structures were found at 20.7 and 24.0 and 26.6 and 29.9 kcal mol^{-1}, combined with $Cl^-\cdot\boldsymbol{S_2}$ and $Cl^-\cdot\boldsymbol{S_3}$, respectively (see Scheme S14 and Fig. S4, S5 and S6 in the ESI†). These three combinations enable the progress of C–H bond activation from the lowest-lying, non-solvated ruthenium precursor $\mathbf{D^+}$ with an activation barrier of only 14.8 kcal mol^{-1}, 6.4 kcal mol^{-1} lower than that calculated by using the pure implicit solvation model. Such a reduction

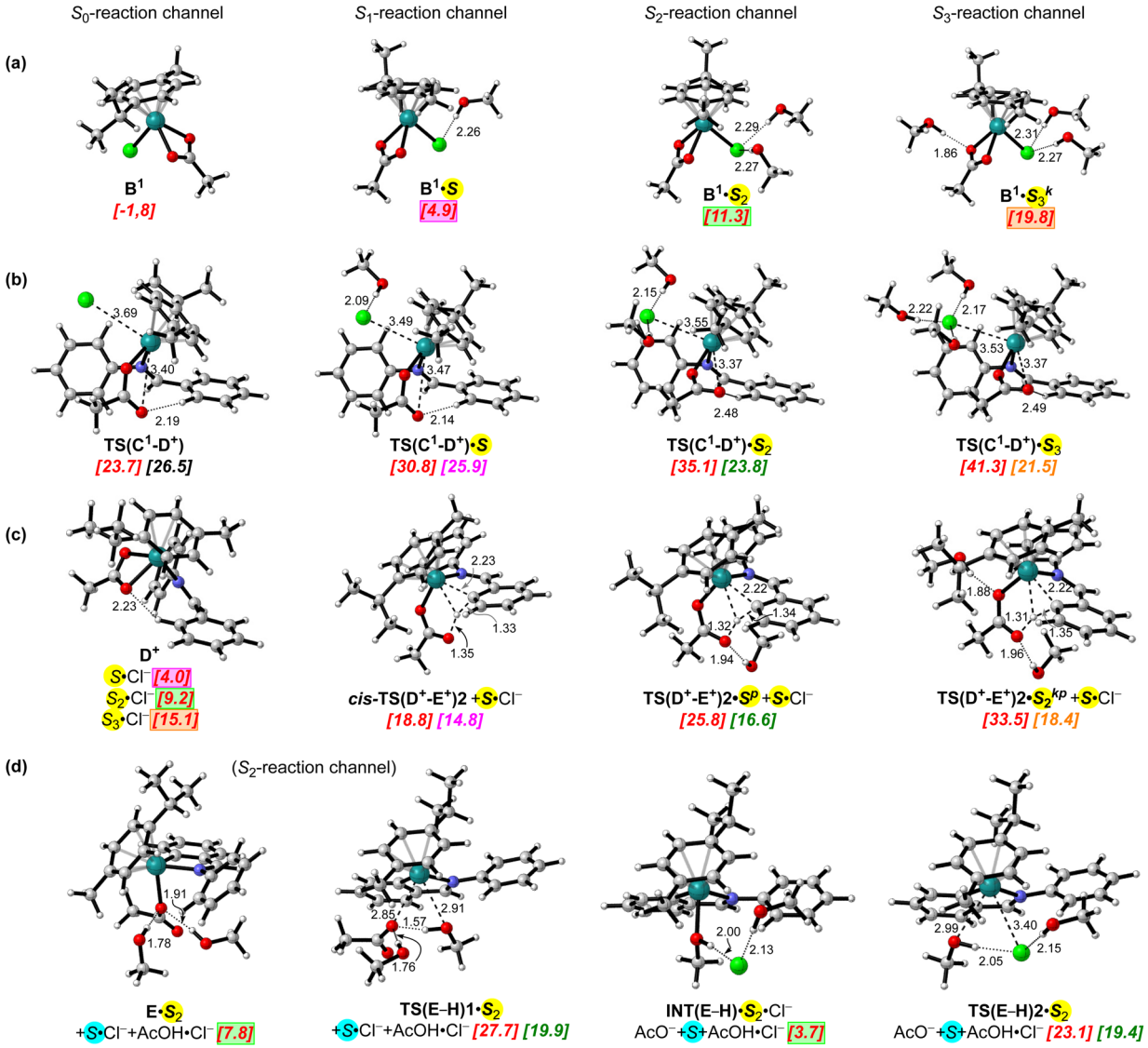

Fig. 2 3D representations of the most significant stationary points located in the S_0-, S_1-, S_2- and S_3-reaction channels. (a) Key chloro acetate (*p*-cymene)ruthenium complexes; (b) TS structures for chloride dissociation from intermediates $\mathbf{C^1}$·$\boldsymbol{S_n}$ leading to cationic intermediate $\mathbf{D^+}$; (c) relevant TS structures for the C–H bond activation process from $\mathbf{D^+}$ to cycloruthenate $\mathbf{E^+}$, (d) TS structures and intermediates for acetate/exchange processes between cycloruthenates **E** and **H**. Quasi-harmonic Gibbs energies calculated at the DLPNO-CCSD(T)/CBS(SMD) level in methanol (298 K, 1 M) after geometry optimizations at the ωB97X-D3/cc-pVDZ-PP[Ru](cPCM) level are shown between brackets, in italics and red, relative to separated reagents (**A** + $\frac{1}{2}\mathbf{B^0}$ + 2AcO$^-$) and an adequate number of explicit solvent molecules to ensure stoichiometric balance. Activation barriers are shown in magenta, green, or orange with respect to the corresponding lowest energy precursors in the S_1-, S_2- or S_3-reaction channels, which are highlighted using the same colours. The hydrogen bonds are represented by dotted lines.

of the activation barrier for the progress of C–H activation *via* the same TS structures is mainly due to the energy balance between non-solvated and solvated precursors and by-products that are introduced into the corresponding continuum model cavities to achieve a realistic description of the system. The lowest-lying TS structures arising from any solvated cationic intermediate $\mathbf{D^+}$·$\boldsymbol{S_n}$ in the S_1-, S_2- or S_3-reaction channels were $\mathbf{TS(D^+\text{-}E^+)2}$·$\boldsymbol{S^p}$, with one MeOH molecule bound to the oxygen atom at the pendant free arm of the acetate moiety, and $\mathbf{TS(D^+\text{-}E^+)2}$·$\boldsymbol{S_2^{kp}}$, with two MeOH molecules H-bonding to both oxygens of the acetate moiety. These transition structures were found in the S_2- and S_3-reaction channels at 25.8 and 33.5 kcal mol^{-1}, respectively, and showed activation energies of 16.6 and 18.4 kcal mol^{-1} from their respective precursors, $\mathbf{D^+}$·$\boldsymbol{S_1}$ and $\mathbf{D^+}$·$\boldsymbol{S_2}$ (see Fig. 2(c) and Schemes S15a and S15b in the ESI†). Other TS structures in the S_2- and S_3-reaction channels involving C–H bond activation by proton-relay mechanisms or deprotonation by an external acetate molecule were found to be higher in energy (see Fig. S5, S6 and S7 in the ESI†).

We have also employed the hybrid explicit/implicit (SMD) solvation model to study the acetate/chloride exchange processes between cycloruthenates **E** and **H**. The energy profiles

calculated at our benchmark level for the S_1- and S_2-reaction channels are included in Fig. S8a and S8b in the ESI.† The most relevant stationary points located in the S_2-reaction channel are depicted in Fig. 2(d). At the DLPNO-CCSD(T)/CBS (SMD) level, the energy barriers for the acetate/chloride exchange processes in the S_1- and S_2-reaction channels differ by less than 1 kcal mol^{-1}. H-Bonding of the second MeOH molecule to the acetate acting as a leaving group increases the activation energy for the methanolysis of the acetate cycloruthenate by *ca.* 1.0 kcal mol^{-1}, from a value of 19.0 kcal mol^{-1} in the S_1-reaction channel *via* **TS(E-H)1·*S*** to a value of 19.9 kcal mol^{-1} in the S_2-reaction channel *via* **TS(E-H)1·*S*$_2$** (see Fig. S8a and S8b in the ESI†). Association of two MeOH molecules to the chloride anion reduces its nucleophilicity, and methanol/chloride exchange in the S_2-reaction channel *via* **TS(E-H)2·*S*$_2$** showed an activation barrier 0.6 kcal mol^{-1} higher than that calculated *via* **TS(E-H)2·*S*** in the S_1-reaction channel. The energy barriers for the acetate/chloride exchange processes in the solvated pathways are estimated to be *ca.* 19.5 and 24.5 kcal mol^{-1} in the forward and reverse directions, respectively. In this manner, mono- or di-solvation of the acetate leaving group led to a reduction of the energy barrier by *ca.* 8.5 kcal mol^{-1}, from the value of 28.5 kcal mol^{-1} previously estimated for the non-solvated ligand exchange process, *via* **TS(E-H)1** (see Fig. S3†). This reduction of the energy barrier is mainly due to the removal of the entropy cost associated with the binding of methanol molecule(s) and cycloruthenate, which is considered to be an integral part of the barrier for the non-solvated ligand exchange processes (from **E** to **TS(E-H)1**) but not applicable to the solvated reaction channels (from **E·*S*$_n$** to **TS(E-H)1·*S*$_n$**).

It should be noted that the activation barrier calculated for the progress of chloride/acetate ligand exchange in the reverse direction from **INT(E-H)·*S*$_2$**·Cl$^-$ to **E·*S*$_2$** *via* **TS(E-H)1·*S*$_2$** (24.0 kcal mol^{-1}) is almost the same as that required for the RDS in the forward direction, from precursor **B^1·*S*$_2$** to key cationic intermediate **D$^+$** + Cl$^-$·***S*$_2$** *via* **TS(C^1-D$^+$)·*S*$_2$** (23.8 kcal mol^{-1}). Thus, acetate/chloride exchange on cycloruthenates and C–H bond activation on cationic intermediates are calculated to be reversible and kinetically irrelevant processes in MeOH at room temperature.

In conclusion, calculations employing a hybrid explicit/implicit solvation model do not change the main results that were reached using the pure implicit CPCM or SMD solvent models. In any of the S_n-reaction channels the energy barriers for the C–H bond activation process were calculated to be lower than those for the previous anion dissociation step. Thus, chloride dissociation leading to cationic intermediate **D$^+$** *via* **TS(C^1-D$^+$)·*S*$_n$** is the RDS and subsequent C–H bond activation events in the CMD pathways are faster and reversible processes. In addition, calculations with the hybrid explicit–implicit solvation model indicate that 2 or 3 MeOH molecules H-bonding to the chlorine atom increase the aptitude of the solvated chloride to act as a leaving group in the anion dissociation step, in a sort of acid catalysis by the polar protic solvent that accelerates cycloruthenation.

2.4.3 Comparison with experimental results. The main conclusions of our computational analysis compare well with several experimental results. First, the formation of cationic intermediate **D$^+$** by anion dissociation in the RDS, which is followed by a kinetically irrelevant AMLA/CMD C–H activation event, is consistent with (a) the lack of significant experimental isotopic effects (k_H/k_D values close to 1) reported for other acetate-assisted ruthenium-catalyzed C–H activations and functionalizations of *N*-tosylbenzaldimines[10b] or phenylpyrazoles[18] and (b) with the negative slope in the Hammett plot determined by competition experiments for acetate-assisted cycloruthenation of substituted phenylpyrazoles in DCM/MeOH as the solvent.[5g] These experimental results are well correlated with the involvement of **TS(C^1-D$^+$)** or **TS(C^2-D$^+$)** in the RDS, as these TS structures show a minimal C–H bond elongation and lead to the development of positive charge near the reaction center. Second, the similarity between the activation energies calculated for the RDS and for the reversion of the C–H activation process in our model system compare well with (c) the reversibility of the C–H activation event previously reported for the ruthenium-catalyzed hydroarylation[7e] or deuteration[7h] of aromatic carbonyl compounds using imines as TDGs in apolar solvents and (d) with the results of deuterium exchange experiments reported for many other C–H bond ruthenations of arenes equipped with *N*-containing DGs in polar protic solvents such as water, methanol, acetic acid or HFIP.[51] Third, by using the Eyring equation, the activation barriers for the solvated reaction channels in the range of 22–24 kcal mol^{-1} allow the estimation of half-live times of 1–12 hours, which compare well with the reaction times of 5–20 hours reported for the cyclometallation of arylimines with the [Ru(*p*-cymene)$_2$Cl$_2$]$_2$ complex in the presence of 4 equiv. of KOAc per ruthenium dimer complex at room temperature in methanol.[5b,c] In addition, the reduction of the calculated activation energies from 26.5 to *ca.* 22 kcal mol^{-1} when switching from the pure implicit to the explicit/implicit SMD solvation model by considering 2 or 3 MeOH molecules that H-bond to the leaving group in the RDS, in a form of acid catalysis, is consistent with kinetic studies of the reactions of [RuCl$_2$(*p*-cymene)]$_2$ with 2-arylquinazolines in MeOH[5e] and of Ru(OAc)$_2$(arene) complexes with 2-phenylpyridine[36a] and 1-phenylpyrazol[36b] in acetonitrile showing that these reactions are autocatalyzed by the freed AcOH.

As indicated by one of the referees, Ru(II)-catalyzed C–H bond activations and functionalizations of arenes equipped with imines and other nonprotic DG that are promoted by [RuCl$_2$(*p*-cymene)]$_2$ are also frequently conducted in the presence of silver salts of weakly coordinating anions and stoichiometric amounts of base, generally carbonate salts. A comparison of our computational results with experiments conducted with these protocols is also possible. The most common mechanistic proposal for (*p*-cymene)Ru(II)-catalyzed C–H activations that are conducted in the presence of silver salts assumes that the initial chloride/acetate exchange processes on ruthenium precursors (like **B^0** and **B^1**) should take place more easily and that diacetate ruthenium complexes (like **B^2**

and $\mathbf{C^2}$) should become the key active intermediates (see ref. 7*e* as an example). In this situation the involvement of TS structures like **TS($\mathbf{C^1}$-$\mathbf{D^+}$)** is precluded but, according to our computational results, **TS($\mathbf{C^2}$-$\mathbf{D^+}$)** would offer the lowest energy pathway for acetate dissociation. Thus, subsequent AMLA/CMD C–H activation on the corresponding intermediate cationic complexes would also be faster and reversible processes. Several studies have postulated that the role played by stoichiometric bases in experimental catalytic protocols is to deprotonate the AcOH moiety of the first cycloruthenate intermediate (like $\mathbf{E^+}$) to form a more stable OAc adduct (like **E**). Thus, for processes that are conducted in the presence of silver salts or with an excess of base, the thermodynamics of the acetate/ligand exchange at the ruthenacycle intermediates could be affected. In particular, association of chloride to acetic acid should be suppressed but, in our opinion, comparison with or inference from our main computational results (regarding (a) binding of a substrate with a nonprotic DG to ruthenium, (b) anion dissociation accelerated by H-bonding to protic polar solvent molecules and leading to key cationic intermediate $\mathbf{D^+}$ as the RDS and (c) subsequent reversible AMLA/CMD C–H activation events) should not be compromised.

3. Conclusions

The reaction mechanisms for the acetate-assisted C–H activation of *N*-phenyl benzaldimine at Ru(*p*-cymene)$_2$Cl$_2$ in methanol have been computationally studied at the DLPNO-CCSD(T)/CBS(CPCM and SMD) level. The most favourable reaction pathway involves the coordination of the imine to the ruthenium precursor followed by ligand dissociation and formation of a cationic ruthenium intermediate as the RDS of the process. Subsequent C–H bond activation events are faster and reversible processes. Two or three MeOH molecules H-bonding to chlorine in the anion dissociation step may speed up the cycloruthenation process, in a sort of acid catalysis by the polar protic solvent. Solvent assistance accelerates the final chloride/acetate ligand exchange process at the cationic cycloruthenate intermediate, particularly when solvent compression in the condensed phase is taken into consideration. Neutral diacetate ruthenium intermediates lead to TS structures of lower energy for the AMLA/CMD C–H bond activation, which result not productive due to higher energy barriers for the ligand exchange processes at acetate ruthenium precursors in MeOH solution. Energy evaluations with hybrid DFT methods (PBE0-D3(BJ), M06-2X or ωB97M-V) failed to reproduce the energy gap between the pathways involving cationic and neutral ruthenium intermediates. In this manner, the use of double-hybrid functionals in combination with dispersion energy corrections was found to be necessary for an accurate evaluation of the kinetics of this acetate-assisted cycloruthenation at the DFT level. Energy evaluations at the PWPB95 + D3(BJ)/aug-cc-pVTZ-PP[Ru](CPCM) level reproduce the DLPNO-CCSD(T)/CBS(CPCM) results at a small fraction of their computational cost and should be reliable for the study of new synthetically useful C–H bond activations/functionalizations involving (*N*,*C*)-cyclometallated (*p*-cymene)Ru(II) complexes in polar protic media. We are currently working on the application of this computational scheme to understand the regioselectivity shown by arenes equipped with *N*-containing DGs in their acetate-assisted cyclometallations at [RuCl$_2$(*p*-cymene)]$_2$.

Author contributions

V. O. performed the computational calculations. The manuscript was written through contributions of both authors. Both authors have given approval to the final version of the manuscript.

Conflicts of interest

There are no conflicts to declare.

Acknowledgements

The authors thank the Centro de Supercomputación de Galicia (CESGA) for providing computer facilities. Funding for open access charge from Universidade da Coruña/CISUG is acknowledged.

References

1 P. B. Arockiam, C. Bruneau and P. H. Dixneuf, *Chem. Rev.*, 2012, **112**, 5879–5918.
2 L. Ackermann, *Chem. Rev.*, 2011, **111**, 1315–1345.
3 N. Kaplaneris, M. Vilches-Herrera, J. Wu and L. Ackermann, *ACS Sustainable Chem. Eng.*, 2022, **10**(21), 6871–6888.
4 For reviews on.(*a*) Annulations of alkynes, seeL. Ackermann, *Acc. Chem. Res.*, 2014, **47**, 281–295; (*b*) Arylations, see P. Nareddy, F. Jordan and M. Szostak, *ACS Catal.*, 2017, **7**, 5721–5745; (*c*) Olefinations, see R. Manikandana and M. Jeganmohan, *Chem. Commun.*, 2017, **53**, 8931–8947. For a relevant sulfonation, see: (*d*) P. Marcé, A. J. Paterson, M. F. Mahon and C. G. Frost, *Catal. Sci. Technol.*, 2016, **6**, 7068–7076 For recent examples on annulation by 1,3-diyne insertion, see: (*e*) G. S. Sontakke, C. Ghosh, K. Pal and C. M. R. Volla, *J. Org. Chem.*, 2022, **87**, 14103–14114; (*f*) Y. Luo and L. Dong, *J. Org. Chem.*, 2022, **87**, 5577–5591 For a recent alkenylation, see: (*g*) C. N. Shambhavi and M. Jeganmohan, *Org. Lett.*, 2023, **25**, 358–363.
5 (*a*) D. L. Davies, O. Al-Duaij, J. Fawcett, M. Giardiello, S. T. Hilton and D. R. Russell, *Dalton Trans.*, 2003, 4132–4138; (*b*) B. Li, T. Roisnel, C. Darcel and P. H. Dixneuf, *Dalton Trans.*, 2012, **41**, 10934–10937; (*c*) B. Li, C. Darcel, T. Roisnel and P. H. Dixneuf, *J. Organomet. Chem.*, 2015,

793, 200–209; (*d*) W.-G. Jia, T. Zhang, D. Xie, Q.-T. Xu, S. Ling and Q. Zhang, *Dalton Trans.*, 2016, **45**, 14230–14237; (*e*) P. Kuzman, F. Pozgan, A. Meden, J. Svete and B. Stefane, *ChemCatChem*, 2017, **9**, 3380–3387; (*f*) C. A. Riedl, L. S. Flocke, M. Hejl, A. Roller, M. H. M. Klose, M. A. Jakupec, W. Kandioller and B. K. Keppler, *Inorg. Chem.*, 2017, **56**, 528–541; (*g*) R. A. Alharis, C. L. McMullin, D. L. Davies, K. Singh and S. A. Macgregor, *Faraday Discuss.*, 2019, **220**, 386–403.

6 (*a*) O. Saidi, J. Marafie, A. E. W. Ledger, P. M. Liu, M. F. Mahon, G. Kociok-Köhn, M. K. Whittlesey and C. G. Frost, *J. Am. Chem. Soc.*, 2011, **133**, 19298–19301; (*b*) R. K. Chinnagolla, S. Pimparkar and M. Jeganmohan, *Org. Lett.*, 2012, **14**, 3032–3035; (*c*) N. Hofmann and L. Ackermann, *J. Am. Chem. Soc.*, 2013, **135**, 5877–5884; (*d*) J. Li, S. Warratz, D. Zell, S. D. Sarkar, E. E. Ishikawa and L. Ackermann, *J. Am. Chem. Soc.*, 2015, **137**, 13894–13901; (*e*) C. Yuan, L. Zhu, R. Zeng, Y. Lan and Y. Zhao, *Angew. Chem., Int. Ed.*, 2018, **57**, 1277–1281; (*f*) L. Zhang, K. Deng, G. Wu, J. Yang, S. Tang, X. Fu, C. Xia and Y. Ji, *J. Org. Chem.*, 2020, **85**, 12670–12681; (*g*) P. Piehl, R. Amuso, A. Spannenberg, B. Gabriele, H. Neumann and M. Beller, *Catal. Sci. Technol.*, 2021, **11**, 2512–2517; (*h*) X. Tan, X. Hou, T. Rogge and L. Ackermann, *Angew. Chem., Int. Ed.*, 2021, **60**, 4619–4624; (*i*) Y.-X. Xu, Y.-Q. Liang, Z.-J. Cai and S.-J. Ji, *Org. Lett.*, 2022, **24**, 2601–2606; (*j*) P. M. Illam and A. Rit, *Catal. Sci. Technol.*, 2022, **12**, 67–74; (*k*) J. M. Zakis, T. Smejkal and J. Wencel-Delord, *Chem. Commun.*, 2022, **58**, 483–490 and references cited therein. (*l*) M. T. Findlay, P. Domingo-Legarda, G. McArthur, A. Yen and I. Larrosa, *Chem. Sci.*, 2022, **13**, 3335–3362 and references cited therein. (*m*) M. T. Findlay, A. S. Hogg, J. J. Douglas and I. Larrosa, *Green Chem.*, 2023, **25**, 2394–2400; (*n*) C.-Y. Shi, X.-Q. Chen, R. Zeng, H. Lu, Z. Fan and A. Zhang, *Org. Lett.*, 2023, **25**, 3870–3875; (*o*) D. M. N. Udayanga, N. Le, E. N. Schwirian, B. Donnadieu, K. Nash, W. Collier, C. E. Webster and X. Cui, *Org. Lett.*, 2023, **25**, 8745–8750 For recent articles on the biological activity of chloro(*p*-cymene)cycloruthenates, see: (*p*) C. A. Riedl, L. S. Flocke, M. Hejl, A. Roller, M. H. M. Klose, M. A. Jakupec, W. Kandioller and B. K. Keppler, *Inorg. Chem.*, 2017, **56**, 528–541; (*q*) C. A. Riedl, M. Hejl, M. H. M. Klose, A. Roller, M. A. Jakupec, W. Kandioller and B. K. Keppler, *Dalton Trans.*, 2018, **47**, 4625–4638; (*r*) P. Getreuer, L. Marretta, E. Toyoglu, O. Dömötör, M. Hejl, A. Prado-Roller, K. Cseh, A. A. Legin, M. A. Jakupec, G. Barone, A. Terenzi, B. K. Keppler and W. Kandioller, *Dalton Trans.*, 2024, **53**, 5567–5579.

7 For recent reviews, see: (*a*) T. Bhattacharya, S. Pimparkar and D. Maiti, *RSC Adv.*, 2018, **8**, 19456–19464; (*b*) J. I. Higham and J. A. Bull, *Org. Biomol. Chem.*, 2020, **18**, 7291–7315, and. (*c*) C. Jacob, B. U. W. Maes and G. Evano, *Chem. – Eur. J.*, 2021, **27**, 13899–13952 For significative examples of imines as TDGs in C–H bond functionalizations catalyzed by (*p*-cymene)ruthenium(II) complexes, see: (*d*) F. Li, Y. Zhou, H. Yang, D. Liu, B. Sun and F.-L. Zhang, *Org. Lett.*, 2018, **20**, 146–149; (*e*) Z.-Y. Li, H. H. C. Lakmal, X. Qian, Z. Zhu, B. Donnadieu, S. J. McClain, X. Xu and X. Cui, *J. Am. Chem. Soc.*, 2019, **141**, 15730–15736; (*f*) G. Li, Q. Liu, L. Vasamsetty, W. Guo and J. Wang, *Angew. Chem., Int. Ed.*, 2020, **59**, 3475–3479; (*g*) Y. Wu, N. Liu, M. Qi, H. Qiao, X. Lu, L. Ma, Y. Zhou and F.-L. Zhang, *Org. Lett.*, 2021, **23**, 3923–3927; (*h*) S. Kopf, F. Ye, H. Neumann and M. Beller, *Chem. – Eur. J.*, 2021, **27**, 9768–9773; see also ref. 6*o*.

8 (*a*) S. Oi, Y. Ogino, S. Fukita and Y. Inoue, *Org. Lett.*, 2002, **4**, 1783–1785; (*b*) B. Li, C. B. Bheeter, C. Darcel and P. H. Dixneuf, *ACS Catal.*, 2011, **1**, 1221–1224; (*c*) B. Li, K. Devaraj, C. Darcel and P. H. Dixneuf, *Tetrahedron*, 2012, **68**, 5179–5184.

9 (*a*) L. Ackermann, P. Novák, R. Vicente and N. Hofmann, *Angew. Chem., Int. Ed.*, 2009, **48**, 6045–6048; (*b*) L. Ackermann, N. Hofmann and R. Vicente, *Org. Lett.*, 2011, **13**, 1875–1877; (*c*) J. Li, K. Korvorapun, S. De Sarkar, T. Rogge, D. J. Burns, S. Warratz and L. Ackermann, *Nat. Commun.*, 2017, **8**, 15430.

10 For representative annulations by alkene hydroarylation of imines see ref. 7*e* and 7*f*. For representative annulations by cycloaddition on imines see: (*a*) M. Tamizmani, B. Ramesh and M. Jeganmohan, *J. Org. Chem.*, 2018, **83**, 3746–3755 For representative annulations by alkyne insertions on arylimines, see: (*b*) C.-H. Hung, P. Gandeepan and C.-H. Cheng, *ChemCatChem*, 2014, **6**, 2692–2697; (*c*) J. Li and L. Ackermann, *Tetrahedron*, 2014, **70**, 3342–3348.

11 R. Manoharan and M. Jeganmohan, *Eur. J. Org. Chem.*, 2016, 4013–4019.

12 For reviews on computational studies on C–H bond activation by metal species, see: (*a*) Y. Boutadla, D. L. Davies, S. A. Macgregor and A. I. Poblador-Bahamonde, *Dalton Trans.*, 2009, 5820–5831; (*b*) D. Balcells, E. Clot and O. Eisenstein, *Chem. Rev.*, 2010, **110**, 749–823; (*c*) D. Balcells and O. Eisenstein, Theoretical Studies on the Reaction Mechanism of Metal-Assisted C–H Activation, in *Comprehensive Inorganic Chemistry II*, ed. J. R. Poeppelmeier, Elsevier, Amsterdam, 2013, vol. 9, pp. 695–726.

13 I. Özdemir, S. Demir, B. Çetinkaya, C. Gourlaouen, F. Maseras, C. Bruneau and P. H. Dixneuf, *J. Am. Chem. Soc.*, 2008, **130**, 1156–1157.

14 (*a*) M. Lafrance, S. I. Gorelsky and K. Fagnou, *J. Am. Chem. Soc.*, 2007, **129**, 14570–14571; (*b*) S. I. Gorelsky, D. Lapointe and K. Fagnou, *J. Am. Chem. Soc.*, 2008, **130**, 10848–10849.

15 D. L. Davies, S. M. A. Donald and S. A. Macgregor, *J. Am. Chem. Soc.*, 2005, **127**, 13754–13755.

16 For systems in which the more electron-rich substrates show increased reactivity and the dominant process should be of electrophilic character, related terms such as "base-assisted internal electrophilic substitution" (BIES, see ref. 16*a* and 16*d*) or "electrophilic-CMD" (eCMD, see ref. 16*b* and 16*c*) have been coined (*a*) W. Ma, R. Mei, G. Tenti and L. Ackermann, *Chem. – Eur. J.*, 2014, **20**, 15248–15251; (*b*) E. Tan, O. Quinonero, M. Elena de Orbe and

A. M. Echavarren, *ACS Catal.*, 2018, **8**, 2166–2172; (*c*) L. Wang and B. P. Darrow, *ACS Catal.*, 2019, **9**, 6821–6836; (*d*) T. Rogge, J. C. A. Oliveira, R. Kuniyil, L. Hu and L. Ackermann, *ACS Catal.*, 2020, **10**, 10551–10558.

17 Computational studies on carboxylate-assisted C–H activation and functionalization by ruthenium(II) complexes have been reviewed, see: (*a*) D. L. Davies, S. A. Macgregor and C. L. McMullin, *Chem. Rev.*, 2017, **117**, 8649–8709; (*b*) C. Shan, L. Zhu, L.-B. Qu, R. Bai and Y. Lan, *Chem. Soc. Rev.*, 2018, **47**, 7552–7576.

18 A. G. Algarra, W. B. Cross, D. L. Davies, Q. Khamker, S. A. Macgregor, C. L. McMullin and K. Singh, *J. Org. Chem.*, 2014, **79**, 1954–1970. See also ref. 5*g*.

19 S. Ruiz, P. Villuendas, M. A. Ortuño, A. Lledós and E. P. Urriolabeitia, *Chem. – Eur. J.*, 2015, **21**, 8626–8636.

20 (*a*) A. Gray, A. Tsybizova and J. Roithova, *Chem. Sci.*, 2015, **6**, 5544–5553; (*b*) L. Zhang, L. Yu, J. Zhou and Y. Chen, *Eur. J. Org. Chem.*, 2018, 5268–5277.

21 J. A. Leitch, P. B. Wilson, C. L. McMullin, M. F. Mahon, Y. Bhonoah, I. H. Williams and C. G. Frost, *ACS Catal.*, 2016, **6**, 5520–5529.

22 M. Zhang and G. Huang, *Chem. – Eur. J.*, 2016, **22**, 9356–9365.

23 (*a*) J.-L. Yu, S.-Q. Zhang and X. Hong, *J. Am. Chem. Soc.*, 2017, **139**, 7224–7243; (*b*) S. Jambu, M. Tamizmani and M. Jeganmohan, *Org. Lett.*, 2018, **20**, 1982–1986 For benzoate-assisted process, see: (*c*) N. Y. P. Kumar, T. Rogge, S. R. Yetra, A. Bechtoldt, E. Clot and L. Ackermann, *Chem. – Eur. J.*, 2017, **23**, 17449–17453; (*d*) M. Simonetti, R. Kuniyil, S. A. Macgregor and I. Larrosa, *J. Am. Chem. Soc.*, 2018, **140**, 11836–11847; (*e*) For a trifluoroacetate-assisted process, see: L. Zhang, L.-L. Wang and D.-C. Fang, *ACS Omega*, 2022, **7**, 6133–6141.

24 P. Chen, Y. Sun, Y. Wu, L. L. Liu, J. Zhu and Y. Zhao, *Org. Chem. Front.*, 2017, **4**, 1482–1492.

25 (*a*) Q. Bu, T. Rogge, V. Kotek and L. Ackermann, *Angew. Chem.*, 2018, **130**, 773–776; (*b*) R. Sivasakthikumaran, S. Jambu and M. Jeganmohan, *J. Org. Chem.*, 2019, **84**, 3977–3989.

26 (*a*) B. Ling, Y. Liu, Y.-Y. Jiang, P. Liu and S. Bi, *Organometallics*, 2019, **38**, 1877–1886; (*b*) B. Lian, L. Zhang and D.-C. Fang, *Org. Chem. Front.*, 2019, **6**, 2600–2606; (*c*) W. Yan, Q. Cheng, Y. Jiao, C.-T. Cao and Z. Tang, *J. Org. Chem.*, 2023, **88**, 14945–14952; (*d*) S. Sau, K. Mukherjee, K. Kondalarao, V. Gandon and A. K. Sahoo, *Org. Lett.*, 2023, **25**, 7667–7672; (*e*) See also the ESI for ref. 25*a*. For related DFT studies on benzimidates and phenylisoindolinone see: (*f*) A. Anukumar, M. Tamizmani and M. Jeganmohan, *J. Org. Chem.*, 2018, **83**, 8567–8580; (*g*) Y.-C. Yuan, Q.-L. Lu, X.-T. Zhu, S. Posada-Pérez, M. Solà, A. Poater, T. Roisnel and R. Gramage-Doria, *Org. Chem. Front.*, 2023, **10**, 42–53.

27 (*a*) A. Schischko, N. Kaplaneris, T. Rogge, G. Sirvinskaite, J. Son and L. Ackermann, *Nat. Commun.*, 2019, **10**, 3553; (*b*) C. Deng, P. Hu, Y. Wang, S. Wang and W. Zhang, *Dalton Trans.*, 2019, **48**, 9181–9186.

28 M. Zhang, J. Zhang, Z. Teng, J. Chen and Y. Xia, *Front. Chem.*, 2020, **8**, 648, DOI: **10.3389/fchem.2020.00648**.

29 (*a*) B. Ling, J. Wang, Y. Liu, Y.-Y. Jiang, P. Liu, J. Feng and S. Bi, *Eur. J. Org. Chem.*, 2021, 266–273; (*b*) H.-J. Long, L. Zhang, B. Lian and D.-C. Fang, *Org. Chem. Front.*, 2022, **9**, 1056–1064.

30 L. A. Machado, E. R. S. Paz, M. H. Araujo, L. D. Almeida, I. A. O. Bozzi, G. G. Dias, C. L. M. Pereira, L. F. Pedrosa, F. Fantuzzi, F. T. Martins, L. A. Cury and E. N. da Silva, *Eur. J. Org. Chem.*, 2022, e202200590.

31 For substrates featuring a protic DG, anion dissociation may be facilitated by proton transfer and HX departure leading to neutral intermediates (contact ion-pairs) with only one acetate ligand, see Scheme S1 at the ESI† and ref. 18, 22, 23*a*, 24, 26*a–c* and 29.

32 K. R. Bettadapur, V. Lanke and K. R. Prabhu, *Org. Lett.*, 2015, **17**, 4658–4661.

33 (*a*) J. McIntyre, I. Mayoral-Soler, P. Salvador, A. Poater and D. J. Nelson, *Catal. Sci. Technol.*, 2018, **8**, 3174–3182; (*b*) C. L. McMullin, N. A. Rajabi and J. S. Hammerton, *Org. Biomol. Chem.*, 2019, **17**, 6678–6686; (*c*) T. Rogge and L. Ackermann, *Angew. Chem., Int. Ed.*, 2019, **58**, 15640–15645; (*d*) X. Chen, H. C. Gülen, J. Wu, Z.-J. Zhang, X. Hong and L. Ackermann, *Angew. Chem., Int. Ed.*, 2023, **62**, e202302021.

34 DFT studies covering the C–H bond activation/functionalization processes of arenes featuring a protic directing group (derived from pyrazol, naphtol, benzoic acid, hydroxychromone, or benzamide) reported lower barriers for the initial ligand dissociation at ruthenium (termed as O–H or N–H activation processes) than those calculated for the subsequent C–H activation events (see ref 18, 22, 23*e*, 26*b*, 26*c*, 26*d*, 27*b*, 29*a* and 29*b*). For the ruthenium-catalyzed annulation of benzamide and propargyl alcohol the opposite was true and the initial N–H activation (accompanied with release of HOAc) was calculated higher in energy than the subsequent C–H activation event (see ref. 26*a*). In addition, concerted ligand dissociation and C–H activation has been reported for phenylpyridines or hydroxychromones (see ref. 20b, 26*b*, 29*a* and 29*b*). Conversely, in previous computational studies on the C–H activation/functionalization processes of arenes equipped with a non-protic DG the kinetic relevance of the dissociation step leading to the key cationic ruthenium intermediates was overlooked (see ref. 5*g*, 21, 24, and 26*d*). In reference 5*g*, the activation energies of the final acetate/chloride ligand exchange processes on ruthenacyclic intermediates were also not evaluated. For other studies in which the C–H activation event was reported as kinetically irrelevant and subsequent functionalization was found as the turnover-limiting step in the catalytic cycle, the computational assessment of the initial ligand exchange processes leading to the key neutral or cationic ruthenium intermediates was also overlooked (see ref. 23*a*, 23*b*, 23*c*, 25*a*, 25*b*, 27*a* and 28).

35 During the preparation of this manuscript an experimental and DFT study on ruthenium(II)-catalyzed C–H activation and intramolecular hydroarylation of transient imines of indole derivatives has been published, see ref. 6*o*. For pre-

vious geometry optimizations and thermochemical evaluations on cycloruthenates derived from *N*-sulfonyl-benzaldimines, see ref. 10*a*. For previous computational studies of acetate-assisted C–H activations of imines at rhodium, iridium, or palladium, see: (*a*) D. L. Davies, S. M. A. Donald, O. Al-Duaij, J. Fawcett, C. Little and S. A. Macgregor, *Organometallics*, 2006, **25**, 5976–5978; (*b*) L. Li, W. W. Brennessel and W. D. Jones, *Organometallics*, 2009, **28**, 3492–3500; (*c*) K. J. T. Carr, D. L. Davies, S. A. Macgregor, K. Singh and B. Villa-Marcos, *Chem. Sci.*, 2014, **5**, 2340–2346; (*d*) J. Li, W. Hu, Y. Peng, Y. Zhang, J. Li and W. Zheng, *Organometallics*, 2014, **33**, 2150–2159; (*e*) L. Zhang and D.-C. Fang, *J. Org. Chem.*, 2016, **81**, 7400–7410.

36 For detailed kinetic studies on acetate-assisted C–H activations of arenes equipped with N-containing DGs, see: (*a*) E. Ferrer Flegeau, C. Bruneau, P. H. Dixneuf and A. Jutand, *J. Am. Chem. Soc.*, 2011, **133**, 10161–10170; (*b*) I. Fabre, N. von Wolff, G. Le Duc, E. Ferrer Flegeau, C. Bruneau, P. H. Dixneuf and A. Jutand, *Chem. – Eur. J.*, 2013, **19**, 7595–7604. See also ref. 5*e*, 6*i*, 10*b*, 18.

37 (*a*) S. Dohm, A. Hansen, M. Steinmetz, S. Grimme and M. P. Checinski, *J. Chem. Theory Comput.*, 2018, **14**, 2596–2608; (*b*) J. M. A. Iron and T. Janes, *J. Phys. Chem. A*, 2019, **123**, 3761–3781.

38 Y. Zhao and D. G. Truhlar, *Theor. Chem. Acc.*, 2008, **120**, 215–241.

39 Y.-S. Lin, G.-D. Li, S.-P. Mao and J.-D. Chai, *J. Chem. Theory Comput.*, 2013, **9**, 263–272.

40 (*a*) C. Riplinger and F. Neese, *J. Chem. Phys.*, 2013, **138**, 034106; (*b*) C. Riplinger, P. Pinski, U. Becker, E. F. Valeev and F. Neese, *J. Chem. Phys.*, 2016, **144**, 024109 The choice of an inexpensive double-ζ basis set for DFT geometry optimizations has a relatively small impact on the DLPNO-CCSD(T) reaction energies and barriers, with differences that are generally much smaller than 1 kcal mol^{-1}, see: M. Wang, X. He, M. Taylor, W. Lorpaiboon, H. Mun and J. Ho, *J. Chem. Theory Comput.*, 2023, **19**, 5036–5046.

41 Calculations with the M06 functional were performed with Gaussian 16 Rev C.01 program (see ESI† for a full citation) while those made with the ωB97X-D3 functional and all the refined single-point energy calculations were performed by using ORCA (version 5.0.3), see. F. Neese, *WIREs Comput. Mol. Sci.*, 2022, **12**, e1606, DOI: **10.1002/wcms.1606**.

42 For recent reviews on hybrid explicit–implicit solvation models, see: (*a*) J. R. Pliego Jr. and J. M. Riveros, *Wiley Interdiscip. Rev.: Comput. Mol. Sci.*, 2020, **10**, 10; (*b*) M. Das, A. R. Gogoi and R. B. Sunoj, *J. Org. Chem.*, 2022, **87**, 1630–1640.

43 (*a*) V. Barone and M. Cossi, *J. Phys. Chem. A*, 1998, **102**, 1995; (*b*) For a review, see: J. Tomasi, B. Mennucci and R. Cammi, *Chem. Rev.*, 2005, **105**, 2999–3093; (*c*) A. V. Marenich, C. J. Cramer and D. G. Truhlar, *J. Phys. Chem. B*, 2009, **113**, 6378–6396.

44 S. Grimme, *Chem. – Eur. J.*, 2012, **18**, 9955–9964.

45 R. Salvio, F. Juliá-Hernández, L. Pisciottani, R. Mendoza-Meroño, S. García-Granda and M. Bassetti, *Organometallics*, 2017, **36**, 3830–3840.

46 **TS(F^c-F)** could not be located at the (B97X-D3/cc-pVDZ-PP [Ru](CPCM) hypersurface. Chart S1 in the ESI† includes a constrained energy profile for the dissociation of the *p*-cymene moiety from F^c leading to **F**.

47 Carbonate has been previously located *trans* to the agostic interaction for the C(sp^3)–H activation of 2-bromoalkylbenzenes promoted by $Pd(OAc)_2$ and $PtBu_3$ as catalysts, see: M. Chaumontet, R. Piccardi, N. Audic, J. Hitce, J.-L. Peglion, E. Clot and O. Baudoin, *J. Am. Chem. Soc.*, 2008, **130**, 15157–15166.

48 Intermolecular deprotonation processes have been found to be favoured over the intramolecular ones in previous computational studies on cycloruthenation of benzylamines in MeOH (see ref. 19) and of 2-phenylpyridines in NMP or dioxane (see ref. 33*a* and 20*b*).

49 Alternative pathway involving neutral bis-imine intermediates and transition structures characterized by a *cis* disposition between the two imine moieties at the ruthenium resulted higher in energy, see ESI,† Scheme S6.† Analogous structures with either a *cis* or a *trans* disposition between the two molecules of the substrate ligated to the ruthenium have been reported for the cyclometallation of 2-phenylpyridines, see ref. 33*b* and 33*c*.

50 CYLview, 1.0b; C. Y. Legault, Université de Sherbrooke, 2009. **https://www.cylview.org** (accessed January 2024).

51 (*a*) Phenylpyridines in D_2O: M. Schinkel, I. Marek and L. Ackermann, *Angew. Chem., Int. Ed.*, 2013, **52**, 3977–3980; (*b*) Phenylbenzimidazoles in TFE (CD_3OD): S. Nunewar, S. Kumar, A. W. Meshram and V. Kanchupalli, *J. Org. Chem.*, 2022, **87**, 13757–13762; (*c*) Phenylisoxazoles in HFIP (D_2O): P. Kumar and M. Kapur, *Chem. Commun.*, 2022, **58**, 4476–4479; (*d*) Indole-carboxamides in TFE: G. K. Das Adhikari, S. R. Mohanty, S. K. Banjare, N. Prusty, G. Murmu and P. C. Ravikumar, *J. Org. Chem.*, 2023, **88**, 952–959; (*e*) Phenyl-imidazo[1,2-*a*]pyridines in AcOH(D_2O): J. A. Tali and R. Shankar, *Org. Lett.*, 2023, **25**, 3200–3205; (*f*) Phenylpyrazolidinones in CD_3OD: see ref. 4*f*.

52 (*a*) A. Sagadevan, A. Charitou, F. Wang, M. Ivanova, M. Vuagnat and M. F. Greaney, *Chem. Sci.*, 2020, **11**, 4439–4443; (*b*) K. Korvorapun, J. Struwe, R. Kuniyil, A. Zangarelli, A. Casnati, M. Waeterschoot and L. Ackermann, *Angew. Chem., Int. Ed.*, 2020, **59**, 18103–18109.

53 R. L. Martin, P. J. Hay and L. R. Pratt, *J. Phys. Chem. A*, 1998, **102**, 3565–3573.

54 A. Karton, A. Tarnopolsky, J.-F. Lamére, G. C. Schatz and J. M. L. Martin, *J. Phys. Chem. A*, 2008, **112**, 12868–12886.

55 A. Tarnopolsky, A. Karton, R. Sertchook, D. Vuzman and J. M. L. Martin, *J. Phys. Chem. A*, 2008, **112**, 3–8.

56 L. Goerigk and S. Grimme, *J. Chem. Theory Comput.*, 2011, **7**, 291–309.

57 (*a*) S. Grimme, J. Antony, S. Ehrlich and H. Krieg, *J. Chem. Phys.*, 2010, **132**, 154104; (*b*) S. Grimme, S. Ehrlich and L. Goerigk, *J. Comput. Chem.*, 2011, **32**, 1456–1465.

58 E. Caldeweyher, S. Ehlert, A. Hansen, H. Neugebauer, S. Spicher, C. Bannwarth and S. Grimme, *J. Chem. Phys.*, 2019, **150**, 154122, DOI: 10.26434/chemrxiv.7430216.v2 (and ChemRxiv 2019).

59 (*a*) H. L. Robinson and M. C. R. Symon, *J. Chem. Soc., Faraday Trans. 1*, 1985, **81**, 2131–2144; (*b*) O. M. Cabarcos, C. J. Weinheimer, T. J. Martínez and J. M. Lisy, *J. Chem. Phys.*, 1999, **110**, 9516–9526; (*c*) T. Megyes, T. Radnai and A. Wakisaka, *J. Phys. Chem. A*, 2002, **106**, 8059–8065; (*d*) T. Megyes, T. Radnay, T. Grózsc and G. Pálinkás, *J. Mol. Liq.*, 2002, **101**, 3–18; (*e*) K. Ozutsumi and H. Ohtaki, *Pure Appl. Chem.*, 2004, **76**, 91–96; (*f*) M. Pagliai, G. Cardini and V. Schettino, *J. Phys. Chem. B*, 2005, **109**, 7475–7481.